

TIC-65910228 b / NGTS-38 b, a 180 day transiting warm super-Jupiter

Toby Rodel^{1*}, Solène Ulmer-Moll^{2,3}, Samuel Gill^{4,5}, Christopher. A. Watson¹, Yoshi Nike Emilia Eschen^{4,5,6}, Alix V. Freckleton⁷, Annelies Mortier⁷, Karen A. Collins⁸, Diana Dragomir⁹, Zahra Essack⁹, Brett Skinner⁹, Niamh Mallaghan¹, Peter J. Wheatley^{4,5}, David R. Anderson¹⁰, Ioannis Apergis^{4,5}, Khalid Barkaoui^{11,12,13}, Matthew P. Battley¹⁴, Daniel Bayliss^{4,5}, François Bouchy³, Edward M. Bryant^{4,5}, Matthew R. Burleigh¹⁵, Benjamin M. J. Cadell¹, Samuel J. Carlier¹⁵, Yann Carteret³, Sarah L. Casewell¹⁵, Alastair B. Claringbold^{4,5}, Jean C. Costes¹, Benjamin D. R. Davies^{4,5}, Lauren Doyle^{4,5}, Phil Evans¹⁶, Jorge Fernández Fernández^{4,5}, Emile Fontanet³, Edward Gillen¹⁴, Michael R. Goad¹⁵, George Harvey¹⁵, Faith Hawthorn^{17,4}, Katlyn L. Hobbs¹, Melissa Hobson³, Giovanni Isopi^{18,19,20,21}, James S. Jenkins^{22,23}, Alicia Kendall¹⁵, David Kipping²⁴, Monika Lendl³, Franco Mallia¹⁹, Christopher Mann²⁵, James McCormac^{4,5}, Ernst J.W. de Mooij¹, Maximiliano Moyano¹⁰, Arianna Nigioni³, Mohammad Odeh¹¹, Vera Maria Passegger^{26,11,27,28}, Suman Saha^{22,23}, Richard P. Schwarz⁸, Amber Sedgley^{4,5}, Avi Shporer²⁹, Abderahmane Soubkiou¹², Stéphane Udry³, Dimitri Veras^{4,5,30}, Jean. P. Vignes³¹, Steven Villanueva Jr.³², José I. Vinés¹⁰, Richard West^{4,5}, Thomas G. Wilson^{4,5}, Hannah L. Worters³³, Mitchell E. Young¹, Aldo Zapparata^{18,19},

Authors' institutions are listed at the end of the paper.

Accepted XXX. Received YYY; in original form ZZZ

ABSTRACT

We present the discovery of TIC-65910228 b / NGTS-38 b, a giant exoplanet with a radius of $1.081 \pm 0.047 R_J$ and a mass of $4.78_{-0.37}^{+0.40} M_J$ on a long-period (180.52791 ± 0.00038 day), moderately eccentric ($e=0.308 \pm 0.011$) orbit transiting a bright ($V=10.230 \pm 0.020$ mag) metal rich ($[Fe/H]=0.33 \pm 0.09$ ‘dex’) F6V-F7V type host star. The planet was initially detected from a single transit in *TESS* Sector 33. A photometric monitoring campaign of 228 nights with NGTS detected a transit egress of the planet, which together with spectroscopic radial velocity monitoring with CORALIE and HARPS identified an orbital period of 180.5 d. These radial velocity measurements also showed the mass of the companion to be planetary. Additional transit observations coordinated by the *TESS* follow-up observing program allowed further confirmation and refinement of this period. With its relatively cool equilibrium temperature of 458 ± 11 K, NGTS-38 b joins a small but growing population of well characterised transiting warm-Jupiters and has one of the longest periods of any discovered to date. The target is situated in the LOPS2 field of the upcoming *PLATO* mission which will allow for greater refinement of the system parameters and potential for the discovery of additional companions too small and/or too long-period to be seen by *TESS* or NGTS. NGTS-38 b’s bright host star and wide orbital separation make it an attractive target for further study, including potential measurement of its spin-orbit alignment or targeted exomoon/ring searches.

Key words: planets and satellites: detection – techniques: photometric – techniques: radial velocities – planets and satellites: individual: TIC-65910228 b

1 INTRODUCTION

Despite the large number of confirmed transiting planets (4520 listed on the NASA Exoplanet Archive; [Akeson et al. 2013; Christiansen et al. 2025](#)¹), periods on the order of tens to hundreds of days remain observationally rare. A relative few ($\lesssim 25\%$) have periods beyond 25

days and even fewer ($\lesssim 5\%$) have periods > 100 days. Many of these $P \geq 100$ days period planets ($\sim 90\%$) were discovered by the *Kepler* mission due to its long observational baseline. However, *Kepler*’s relatively narrow field of view meant that many of these targets orbit faint, distant stars. This limits the extent to which they can be characterised in detail through spectroscopic follow-up observations.

Many of the most pressing questions in exoplanet science require a large sample of well characterised long-period ($\sim 10 - 1000$ days) transiting planets with fully measured masses, radii and orbital solutions. For instance, the existence of close in giant planets, often

* Email: trodel01@qub.ac.uk

¹ Accessed 2026 January 16. Available at: <https://exoplanetarchive.ipac.caltech.edu>

termed ‘hot-Jupiters’ (e.g. 51 Pegasi b; Mayor & Queloz 1995), challenged pre-existing notions of planet formation and evolution (see review; Dawson & Johnson 2018). The existence of these planets can either be explained with in-situ formation (e.g; Bodenheimer et al. 2000) or ex-situ formation followed by inward migration with the latter usually being preferred. Two main migration channels are proposed: high eccentricity migration (Lidov 1962; Kozai 1962; Rasio & Ford 1996) where a dynamical interaction perturbs the planet into an eccentric orbit that is circularised through tidal interactions over time; or disk migration (Goldreich & Tremaine 1980) where interactions with a protoplanetary disk cause a planet to lose angular momentum and migrate inwards.

These migration mechanisms should leave detectable dynamical traces in a planetary system, for instance, the orbital eccentricity and/or the spin-orbit alignment / obliquity between the planet and host star (Naoz 2016; Dawson & Johnson 2018; Albrecht et al. 2022). However, for giant planets with orbital periods of 10 days or shorter, tidal interactions with the star circularise orbits and can dampen obliquities (Albrecht et al. 2012a, 2022) - effectively removing any trace of the system’s dynamical history. Longer-period giant planets (‘warm-Jupiters’) transiting nearby bright stars are therefore valuable tracers of planet formation and migration as spectroscopic radial velocity observations can constrain their undamped orbital eccentricities and obliquities via the Rossiter-McLaughlin effect (RM; Rossiter (1924); McLaughlin (1924); also see Review by Triaud (2018)). Already, RM surveys have found a greater trend towards alignment in giant planets with periods on the order of 10s to 100s of days compared to those with periods shorter than 10 days (Rice et al. 2022; Wang et al. 2024; Espinoza-Retamal et al. 2025). Although the numbers are currently small, this could suggest warm-Jupiters may be a distinct sub-population rather than representing a transitional stage towards becoming hot-Jupiters.

Longer-period planets also generally experience less irradiation from their host stars. This drastically reduces the rates of both atmospheric mass loss (Sanz-Forcada et al. 2011) and inflation (Dawson & Johnson 2018), meaning these planets are more likely to retain their primordial atmospheres and interiors. If the host star is bright, the planetary atmosphere can be probed via transmission spectroscopy (e.g; Charbonneau et al. 2002). These observations can provide additional constraints on planet formation and migration mechanisms using tracers such as the C/O ratio (Öberg et al. 2011), as well as general atmospheric dynamics and compositions at cooler equilibrium temperatures (Fortney et al. 2020).

Long period giant planets are also valuable targets in searches for circumplanetary objects such as exomoons and exorings (Szabó et al. 2024), both of which are expected to become more stable with increasing orbital separation (Barnes & O’Brien 2002; Barnes & Fortney 2004). In addition, as we push to longer-periods, wider separations and cooler equilibrium temperatures, the possibility of either directly habitable exoplanets or habitable moons around giant planets becomes greater.

The Transiting Exoplanet Survey Satellite (*TESS*; Ricker et al. 2015) is specifically designed for the discovery of transiting exoplanets around nearby bright stars. The survey strategy of tiling *TESS*’ wide rectangular field across the sky in ‘sectors’ has led to almost total sky coverage over the primary and extended missions. However, this strategy limits the observational baseline, creating difficulties in detecting long-period planets. Simulation work by Cooke et al. (2018, 2019, 2021); Villanueva et al. (2019) and most recently Rodel et al. (2024) has found that the majority of long-period planets detected via *TESS* will have unsolved periods, these being detected either from a single ‘monotransit’ or ‘duo/triotransits’ with two or three events

separated by the ~ 2 yr gap between *TESS* visits (e.g; Hawthorn et al. 2024). In the former case the period is almost entirely unconstrained, although the duration of transit can give some indication, whilst in the latter case the true period forms part of a sequence of aliases, each an integer fraction of the gap between transits.

This means extensive follow-up observational programs are required to confirm these planets and find their true orbital periods. The Next Generation Transit Survey (NGTS; Wheatley et al. 2018) is one of the best suited instruments for the photometric follow-up of unsolved *TESS* detections. It has already been used to confirm several long-period transiting giant planets (Gill et al. 2020c, 2024; Grieves et al. 2022; Battley et al. 2024; Ulmer-Moll et al. 2022, 2025; Kendall et al. 2025) as well as brown dwarf and late M dwarf companions (Gill et al. 2020a,b, 2022; Lendl et al. 2020; Henderson et al. 2024; Rodel et al. 2025). The Characterising ExOPlanet Satellite (*CHEOPS*; Benz et al. 2021) has similarly been used from space to confirm smaller transiting long-period planets (e.g; Ulmer-Moll et al. 2023; Osborn et al. 2023; Tuson et al. 2023). Spectroscopic radial velocity campaigns using instruments such as CORALIE (Queloz et al. 2001), the Fiberfed Extended Range Optical Spectrograph (FEROS; Kaufer et al. 1999) or the High Accuracy Radial velocity Planet Searcher (HARPS; Pepe et al. 2000; Mayor et al. 2003) are also essential in such follow-up efforts. These observations act either to confirm the mass of a planet with a photometrically determined period, or to provide an initial period that can be confirmed more precisely with additional photometry (e.g. Schlecker et al. 2020; Hobson et al. 2021; Eberhardt et al. 2023; Brahm et al. 2023; Bieryla et al. 2026).

It is in this context that we present the discovery of TIC-65910228 b (which we also refer to as NGTS-38 b): a transiting giant planet on a 180.5 day orbit around a bright F type star. This makes it one of the longest period transiting planets ever found and one of the most amenable of these to characterisation. In Section 2 we describe the initial detection of the planet from a single *TESS* transit (Section 2.1), the detection of an egress with NGTS (Section 2.2), simultaneous observation of the most recent transit from several facilities (Section 2.3), and longer term photometric monitoring (Section 2.4) used to search for rotational signals. In Section 3 we describe the spectroscopic campaigns with CORALIE (Section 3.1) and HARPS (Section 3.2) that allowed a mass measurement of the planet via radial velocity and spectroscopic characterisation of the host star, which we describe in Section 4. In Section 5 we describe the joint global model fit we performed on the previously described data in order to obtain a full orbital solution for NGTS-38 b. Then, in Section 6, we present the parameters derived from our fit alongside some interior structure modelling and discuss their significance. We then discuss the potential for future work on the system in Section 7 before summarising our work with some concluding remarks in Section 8.

2 PHOTOMETRIC OBSERVATIONS

The photometric datasets for TIC-65910228 / NGTS-38 are summarised in Table 1 and they are described in the remainder of this section.

2.1 *TESS*

TESS has been operating a (near) all-sky survey since 2018 aimed at discovering exoplanets transiting bright host stars. *TESS*’ four ~ 10 cm cameras are arranged vertically to provide a rectangular $24^\circ \times 96^\circ$ field of view. *TESS* rotates this field of view around the

Table 1. Summary of photometric observations of NGTS-38.

Facility	Night(s) Observed (UTC)	N_{images}^*	Exptime (s)	N_{nights}^{**}	Filter	Pipeline	$N_{\text{telescopes}}$	Note(s)
WASP-South	2011 Nov 2 - 2012 Mar 29	2464	30	77	WASP	WASP	1	
ASAS-SN	2016 Feb 2 - 2018 Sep 17	795	90	276	V	ASAS-SN	1	
ASAS-SN	2018 Aug 8 - 2025 Nov 23	4544	90	1304	g	ASAS-SN	1	
TESS-S07	2019 Jan 8 - 2019 Feb 16	1086	1800	22.6	TESS	TESS-SPOC	1	
TESS-S33	2020 Dec 18 - 2021 Jan 13	3485	600	24.2	TESS	TESS-SPOC	1	a
TESS-S34	2021 Jan 14 - 2021 Feb 8	3358	600	23.2	TESS	TESS-SPOC	1	
TESS-S61	2023 Jan 18 - 2023 Feb 12	9503	200	23.0	TESS	TESS-SPOC	1	
TESS-S87	2024 Dec 18 - 2025 Jan 14	14576	120	20.2	TESS	SPOC	1	
TESS-S88	2025 Jan 14 - 2025 Feb 11	19432	120	27.0	TESS	SPOC	1	
NGTS	2023 Aug 25 - 2024 Feb 4	118315	10	115	NGTS	BSPROC	1	
NGTS	2024 Apr 16 - 2024 May 12	3012	10	8	NGTS	BSPROC	1	
NGTS	2024 Aug 18 - 2024 Nov 21	44971	10	69	NGTS	BSPROC	1	
NGTS	2024 Nov 22 - 2024 Dec 31	131761	10	36	NGTS	BSPROC	2	b
NGTS	2025 Dec 2 - 2025 Dec 5	22903	10	4	NGTS	BSPROC	4	
LCO-SSO 1m	2025 Dec 4	900	10	1	i'	ASTROIMAGEJ	2	c
LCO-SSO 0.35m	2025 Dec 4	1106	27	1	i'	ASTROIMAGEJ	2	c
LCO-CTIO 1m	2025 Dec 4	1068	10	1	i'	ASTROIMAGEJ	2	d
LCO-CTIO 0.35	2025 Dec 4	652	27	1	i'	ASTROIMAGEJ	1	d
El Sauce	2025 Dec 4	751	32	1	Rc	ASTROIMAGEJ	1	d
DSCO.4m	2025 Dec 4	120	135	1	Chroma R	ASTROIMAGEJ	1	d
OACC - CAO (0.6 m)	2025 Dec 4	196	100	1	i'2	ASTROIMAGEJ	1	d

* For *TESS* N_{images} is counted as the number of individual points in the lightcurve with a data quality flag of 0.

** For *TESS* this is calculated by $(\text{Exptime (s)} \times N_{\text{images}}) / 86400$ s while for all ground based instruments this is simply the count of nights with observations.

a: Full Transit on UTC 2020 December 25. **b:** Transit Egress on UTC 2024 December 8. **c:** Transit Ingress on UTC 2025 December 4. **d:** Transit Egress on UTC 2025 December 4

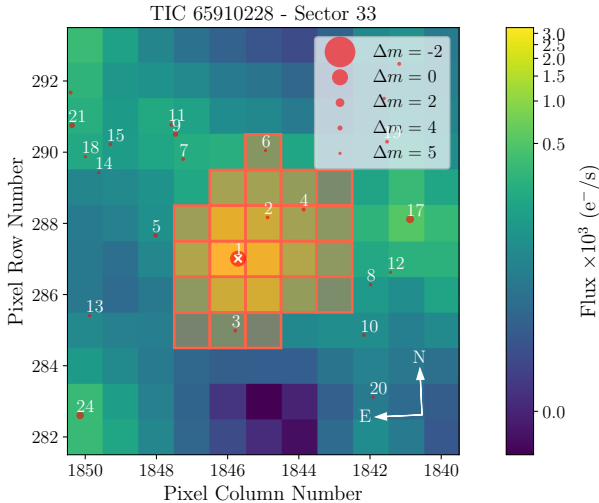


Figure 1. *TESS* target pixel file for NGTS-38 in sector 33. Each red circle represents a *Gaia* source down to a magnitude difference of 6 from the target. The circles are also sized according to the difference in magnitude from the target, which is marked with a white x and numbered 1.

sky in ‘sectors’, which are each observed for ~ 27 days at a time, although overlap between sectors can provide some targets with longer baselines.

NGTS-38 was observed by *TESS* in sectors 7, 33, 34, 61, 87 and 88. We show the sector 33 Target Pixel File created using TPFPLTTER (Aller et al. 2020) in Figure 1. In the most recent two sectors, lightcurves were produced onboard the spacecraft at two minute cadence by the Science Processing Operations Centre (SPOC; Jenkins et al. 2016). The lightcurves for the remaining sectors were produced from the Full Frame Images (FFIs) using the *TESS*-SPOC pipeline

(Caldwell et al. 2020) at cadences of 30-minutes for sector 7, 10-minutes for sectors 33 and 34 and 200-seconds for sector 61. We performed quality cuts on all of these lightcurves, only using data points with a quality flag of 0. We used the PDCSAP_FLUX column for all sectors. These lightcurves are plotted in Figure 2.

A single transit of NGTS-38 b was detected at BJD=2459209.23 (see Figures 2 and 3a) in the Sector 33 *TESS*-SPOC FFI lightcurve by the Single Transit Search (STS) pipeline, a custom algorithm from the *TESS* Single Transit Planet Candidate Working Group (TSTPC WG). The TSTPC WG uses STS to systematically search *TESS*-SPOC lightcurves for single transit events, aiming to increase the yield of *TESS* long-period planets. The STS algorithm, employing ASTROPY Box-Least Squares method (Astropy Collaboration et al. 2022), identified the event by searching for periods near or beyond the *TESS* sector length across a thousand trial durations from 1 hour to 1 day. The transit signal was then compared against a sinusoidal model to exclude the possibility of stellar variability. The resulting data validation report was twice independently vetted, followed by a group evaluation session. The field is crowded (seen in Figure 1), with numerous faint sources within the photometric aperture. However, pixel-level lightcurves generated with ELEANOR (Feinstein et al. 2019) confirmed that the transit source is on-target on NGTS-38. The contaminating sources are too faint ($\Delta m_{\text{TESS}} > 4$) to produce the observed ~ 3 parts per thousand (ppt) transit depth, and no significant centroid motion was detected during the event, ruling them out as the event’s origin. The validated planet candidate parameters were uploaded to ExoFOP-TESS as the final step of TSTPC’s processes. The event in Sector 33 was also detected by the MONOFIND algorithm (Gill et al. 2020a; Hawthorn et al. 2024), independently from and contemporaneously with the TSTPC WG detection.

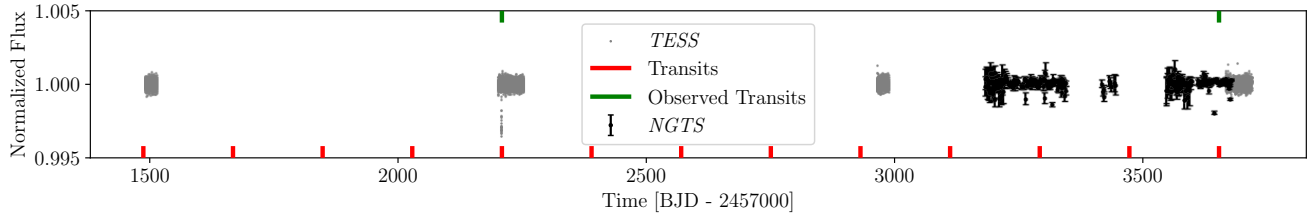


Figure 2. Discovery photometry for NGTS-38 b. All *TESS* lightcurves have been binned to 30 minute cadence for ease of comparison. NGTS data has been binned to nightly cadence and outliers with flux < 0.998 or flux errors > 0.001 removed. Red vertical dashes along the bottom x-axis show the expected transit times. Similar green dashes are shown on the inside of the top x axis to show transits actually covered by the data. The transit predicted at $\text{BJD-2457000} \approx 3292$ does fall within the time limits of the first run of NGTS data but falls within a data gap.

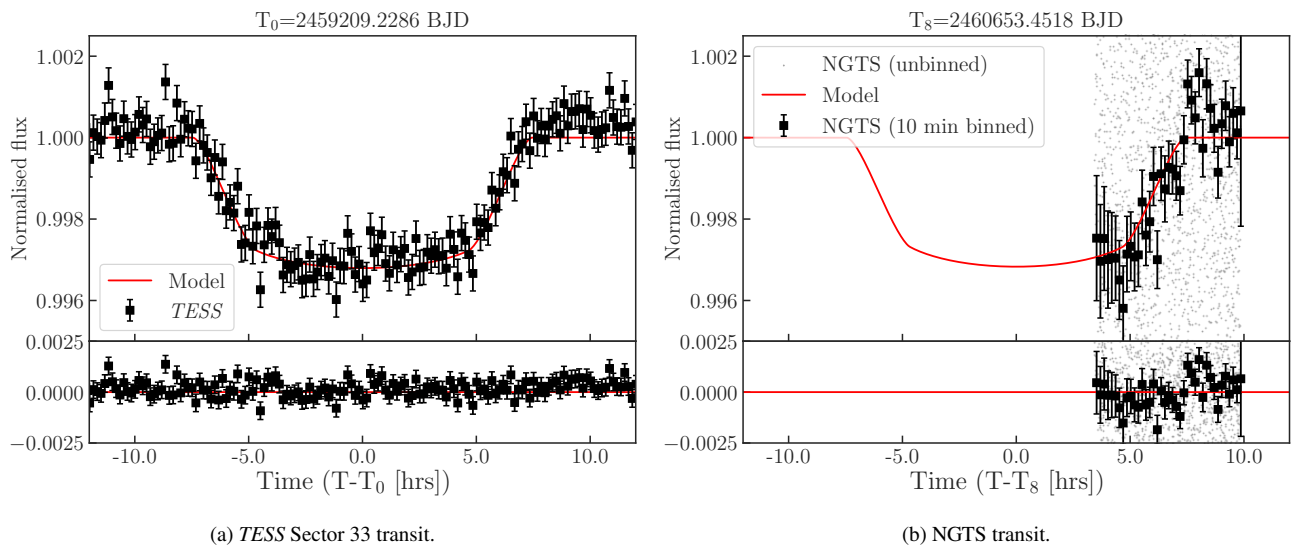


Figure 3. Discovery transit lightcurves of NGTS-38 b. Each panel shows the median transit model (see Section 5) as a solid red line. The transit data plotted is shown as black square markers with errorbars. For NGTS the data are binned to 10-minute cadence to match *TESS* and the unbinned data are shown as gray dots. The top panel of each subfigure shows the data and model while the lower panel of each shows the residuals after the model has been subtracted from the observed data. The *TESS* data shows a systematic ‘bump’ in flux post transit, this is probably an artefact of the PDCSAP_FLUX flattening of the lightcurve. Our own spline fit (see Section 5) failed to remove this but the impact on any fitted parameters is likely to be negligible.

2.2 NGTS

NGTS is a ground based photometric facility made up of twelve individual robotic 20cm telescopes located in Paranal, Chile. Despite being ground based, the precision of NGTS is able to rival or exceed that of *TESS* (Bryant et al. 2020; O’Brien et al. 2022; Bayliss et al. 2022), making it very well suited to photometric follow-up of *TESS* single transit candidates (Bayliss et al. 2020) such as NGTS-38.

NGTS-38 was observed by NGTS in four separate observing campaigns for a total of 228 nights between August of 2023 and January of 2025, these are summarised in Table 1. The first campaign consisted of 115 nights of observation between 2023 August 25 and 2024 February 4. The second brief campaign consisted of 8 nights between 2024 April 16 and 2024 May 12, this sparse coverage was due to technical issues with the NGTS roof control system and cloudy weather. The third campaign began on 2024 August 18 with 69 nights before 2024 November 21. These first three campaigns all used a single telescope while the fourth and final campaign used two simultaneously for 36 nights of observations beginning immediately after the previous on 2024 November 22 and lasting until 2024 December 31.

These data were reduced using the *BSPROC* pipeline as described in Bryant et al. (2020) using fixed comparison stars and apertures

across each run to ensure night to night photometric stability. A sample of the reduced lightcurve data can be found in Table A1. Before any analysis was done, we median normalised the data across each campaign.

We searched the NGTS monitoring data for a second planetary transit using the algorithm described by Gill et al. (2020a), which uses the initial *TESS* detection as a template in a cross-correlation with the NGTS photometry. This revealed a candidate egress event on the night of 2024 December 8, which was confirmed with a visual inspection of the data (see Figure 3b). No other transit events were identified in the 228 nights of NGTS photometry.

With two transits of NGTS-38 b detected, the orbital period of the planet was constrained to a finite set of alias of the time separation of the two transits, which was 1444 d. The majority of these aliases were ruled out by either the *TESS* or NGTS photometry, including all alias periods shorter than 72 d.

The egress event on 2024 December 8 showed a strong systematic increase in flux, comparable to the transit depth, at the beginning of the night, which was coincident with observations at high airmass ($\gtrsim 1.4$). To correct for this, we fit a linear model of flux, f , against airmass, $\text{sec } z$, to the residuals from the template match model against

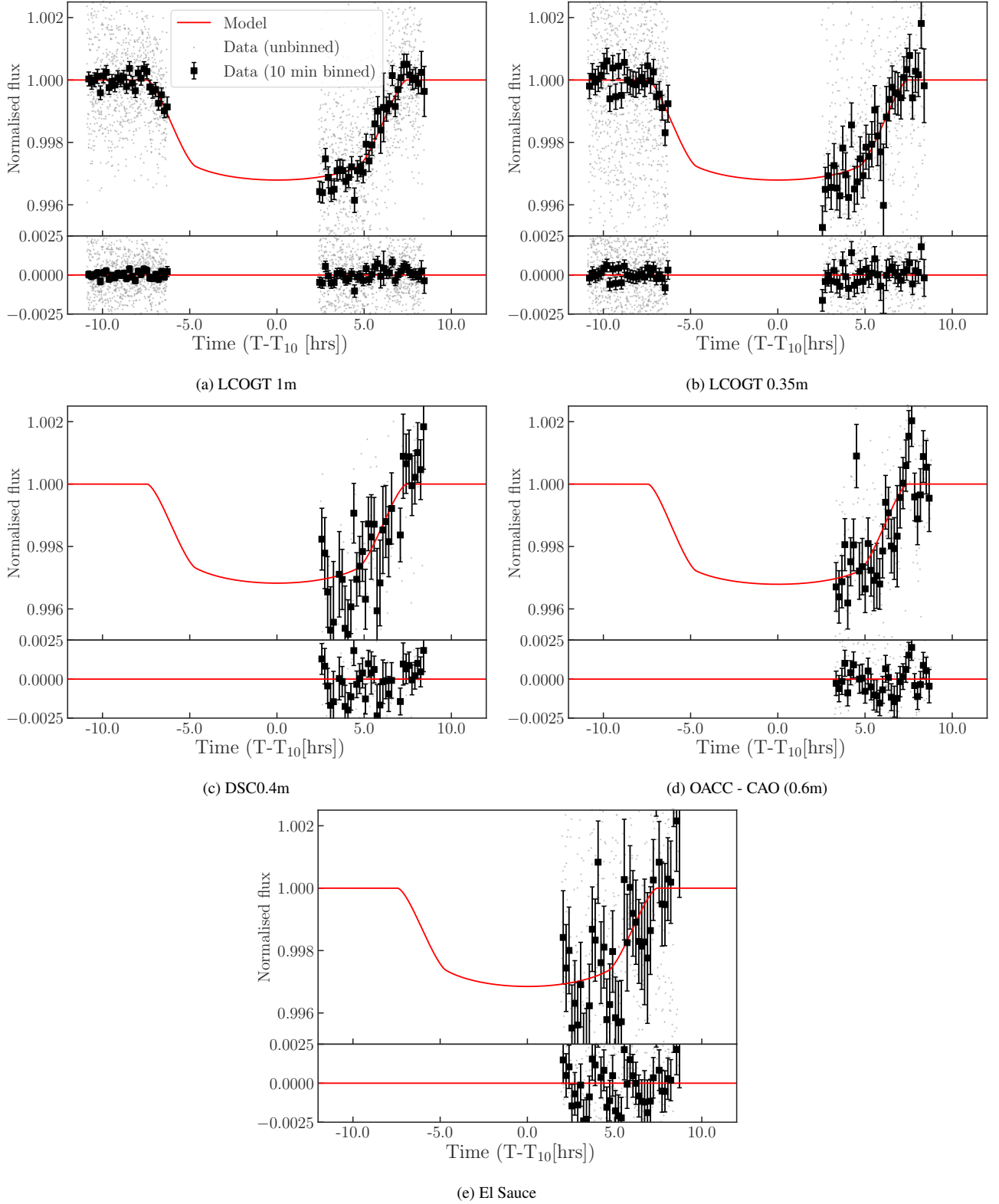


Figure 4. Simultaneous transit lightcurves of NGTS-38 b from the night beginning 2025 December 4 UTC ($T_{10}=2461014.5077$ BJD). Each panel shows the median transit model (see Section 5) as a solid red line. The top panel of each subfigure shows the data and model while the lower panel of each shows the residuals after the model has been subtracted from the observed data. Unbinned data is shown as gray dots while the black squares with error bars represent the data binned to 10 minute cadence. The LCOGT data for the same diameter telescopes from CTIO and SSO have been stitched together to save space but these data were fitted separately.

the data from the night of the transit (2024 December 8). The function took the form $f = C_1 \sec z + C_0$ with the fit resulting in coefficients of $C_1 = 0.00244519$ and $C_0 = -0.00383989$.

We launched a short fifth NGTS campaign from 2025 December 2 to 2025 December 5 with four telescopes to target the 180.5 d alias, which was the best match to our radial velocity observations (see Section 3). However, due to high cloud cover over Paranal at the time we were unable to obtain any usable data.

2.3 TFOP SG1 Observations

After identifying the most likely orbital period for NGTS-38 b of 180.5 d using *TESS* and NGTS photometry (Sects. 2.1 & 2.2) and radial velocity observations (Sect. 3), we sent out a general call to the *TESS* Follow-up Observing Program Sub Group 1 (TFOP SG1; Collins 2019)² to target the predicted transit ingress on the night beginning 2025 December 4 UTC and the egress on 2025 December 5 UTC. Observations were contributed by the Las Cumbres Observatory Global Telescope Network (LCOGT; Section 2.3.1; Brown et al. 2013) *TESS* Follow-up Key Project (PI: Shporer), as well as three private observatories: The Deep Sky Chile 0.4 m (DSC 0.4 m; Section 2.3.2), the Osservatorio Astronomico di Campo Catino (OACC; Section 2.3.3) and the El Sauce Observatory (Section 2.3.4).

Photometric extraction was carried out for all of these instruments with the ASTROIMAGEJ package (Collins et al. 2017). The comparison star ensemble for each lightcurve was selected by minimizing the RMS of the residuals of a simultaneous fit to a transit model and a linear fit to airmass using ASTROIMAGEJ.

The resulting transit light curves are all shown in Figure 4. The detection of this transit ruled out the majority of the remaining alias periods allowed by the *TESS* and NGTS transits (Sect. 2.2 and Fig. 3). The full set of aliases allowed by the combined photometry are: 72, 90, 120, 181 and 361 d. Only the 180.5 d alias is also consistent with our radial velocity observations (see Section 3).

2.3.1 LCOGT

A transit of NGTS-38 b beginning on 2025 December 4 UTC was observed from two Las Cumbres Observatory Global Telescope network nodes. The transit ingress was observed simultaneously with two 1.0 m and two 0.35 m telescopes at the Siding Spring Observatory (SSO) node near Coonabarabran, Australia and the egress was observed simultaneously with two 1.0 m and one 0.35 m telescopes at the Cerro Tololo Inter-American Observatory (CTIO) node in Chile. The 1.0 m telescopes are equipped with 4096×4096 SINISTRO Cameras, with an image scale of 0.389'' per pixel and a field of view (FOV) of 26' × 26'. The 0.35 m Planewave Delta Rho 350 telescopes are equipped with 9576 × 6388 QHY600 CMOS cameras having an image scale of 0''.73 per pixel, resulting in a 114' × 72' full field of view. We used the optional 30' × 30' sub field of view for a faster detector read-out. All observations were carried out in the Sloan-i' filter with exposure times of 10 s and 27 s for the 1.0 m and 0.35 m telescopes, respectively. The image data were calibrated with the standard LCOGT BANZAI pipeline (McCully et al. 2018), and photometric extraction was performed with ASTROIMAGEJ using uncontaminated photometric apertures of 6–9''. We combined all 1.0 m datasets in Figure 4a and all 0.35 m datasets in Figure 4b.

² <https://tess.mit.edu/followup>

2.3.2 DSC 0.4m

The 2025 December 5 UTC egress was also observed from near Ovalle, Chile, with the Deep Sky Chile 0.4 m (DSC 0.4 m) Planewave CDK400 telescope, which was equipped with a QHYCCD600M camera and Chroma R filter (650 nm ± 50 nm). The 9576 x 6388 pixel detector has an image scale of 0.4'' per pixel and a FOV of 62' × 42'. The images were calibrated and photometric data were extracted with ASTROIMAGEJ using circular 5'' photometric apertures. The egress lightcurve is shown in Figure 4c.

2.3.3 OACC - CAO 0.6m

The 2025 December 5 UTC egress was also observed from the Osservatorio Astronomico di Campo Catino (OACC) Campocatino Austral Observatory (CAO) 0.6 m telescope (El Sauce, Atacama desert, Chile) equipped with a Moravian C3-61000EC PRO camera that provides a FOV of 30' × 20' with a pixel scale of 0.2'' per pixel. The images were acquired with a standard photometric Astrodon i'2 filter. The time series, composed of 196 x 100s images, was calibrated and photometric data were extracted with ASTROIMAGEJ using circular 6.8'' photometric apertures. The egress lightcurve is shown in Figure 4d.

2.3.4 El Sauce

The transit egress was also observed from El Sauce observatory in Coquimbo Province, Chile on UTC 2025/12/05 with a CDK500 0.5 m robotic telescope equipped with an Rc filter and a Moravian C3-26000 camera with 6252 x 4176 pixels binned 2 x 2 in-camera resulting in an image scale of 0.449''/pixel. The 751 x 32 s images were calibrated and photometric data were extracted with ASTROIMAGEJ using circular 5.8'' photometric apertures. The egress lightcurve is shown in Figure 4e.

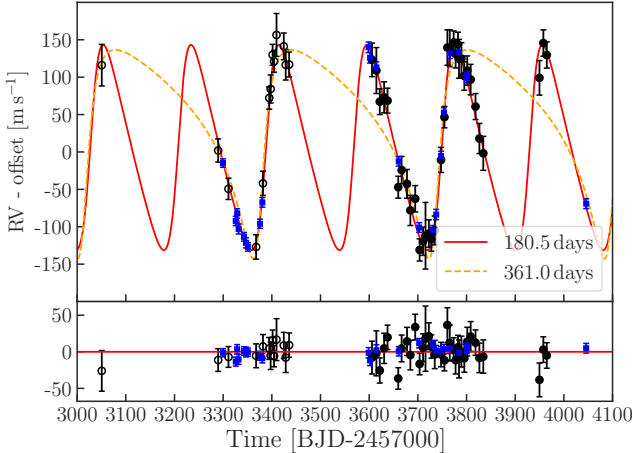
2.4 Archival Photometry

2.4.1 WASP

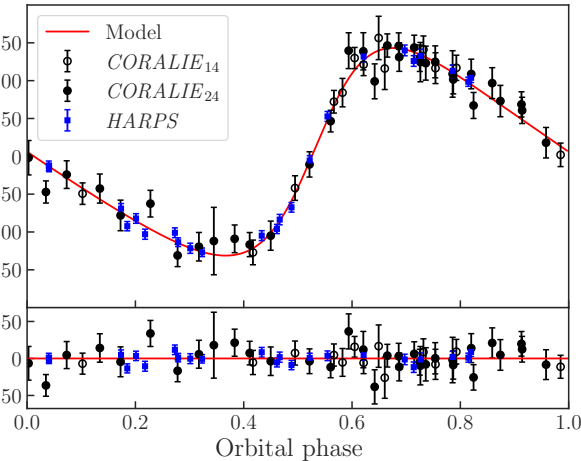
The Wide Angle Search for Planets (WASP; Pollacco et al. 2006) was a ground based transit survey with a northern facility (often simply referred to as WASP) at the Observatorio del Roque de los Muchachos on the island of La Palma in the Canary Islands and a Southern facility (WASP-South) at the Sutherland Station of the South African Astronomical Observatory. Both WASP instruments consisted of eight Canon Telephoto lenses with a ~ 11 cm aperture with custom 2048 × 2048 pixel CCD cameras on a fixed robotic mount, resulting in a wide 482 square degree field of view. NGTS-38 was observed by WASP-South from 2011 November 2 to 2012 March 29. The dataset contains no transit coverage, and the transit is shallower than WASP's ~ 1% detection limit. However, the WASP lightcurve was still used to attempt to measure a photometric rotation period of the star which we present in Section 4.4.1.

2.4.2 ASAS-SN

The All Sky Automated Survey for SuperNovae (ASAS-SN Kochanek et al. 2017) is made up of several stations hosted at various locations around the world by the LCOGT network (see Section 2.3 and 2.3.1). Each station consists of a single Nikon telephoto lens with a 14 cm aperture and an approximately 4.5 square degree field of view. ASAS-SN is a transient survey and so is not well suited for



(a) Radial velocities as a function of time.



(b) Radial velocities after phase-folding on the orbital period.

Figure 5. Radial velocity measurements of NGTS-38 with the fitted radial velocity baseline offset values subtracted (see Section 5 and Table C1). Data points from CORALIE are denoted with black circles with those from the first epoch unfilled and those from the second epoch filled. HARPS data points are shown as blue squares. The median fitted RV model is also overplotted with a red solid while the best fitting model to the 361.0 day period alias is shown with an orange dashed line in the top panel. Subfigure (a) shows the data plotted versus time while (b) shows the same data as a function of orbital phase. For each subfigure, the top panel shows the data and model, while the bottom panel shows the residuals with the model subtracted.

transit detection given the low number of observations per target on a given night, however, its long baseline of nightly coverage does allow for monitoring rotation and/or activity in stars (e.g; Eschen et al. 2025). NGTS-38 was observed by ASAS-SN from 2016 February 2 to 2018 September 17 in the V band and 2018 August 8 to 2025 November 23 in the g band. We apply the same quality cuts as in Eschen et al. (2025) to our dataset in order to use the ASAS-SN lightcurve to search for a stellar rotation signal, which we present in Section 4.4.1.

3 SPECTROSCOPIC OBSERVATIONS

In this section we describe the spectroscopic observations taken of TIC-65910228 / NGTS-38 with CORALIE (Queloz et al. 2001, Sec-

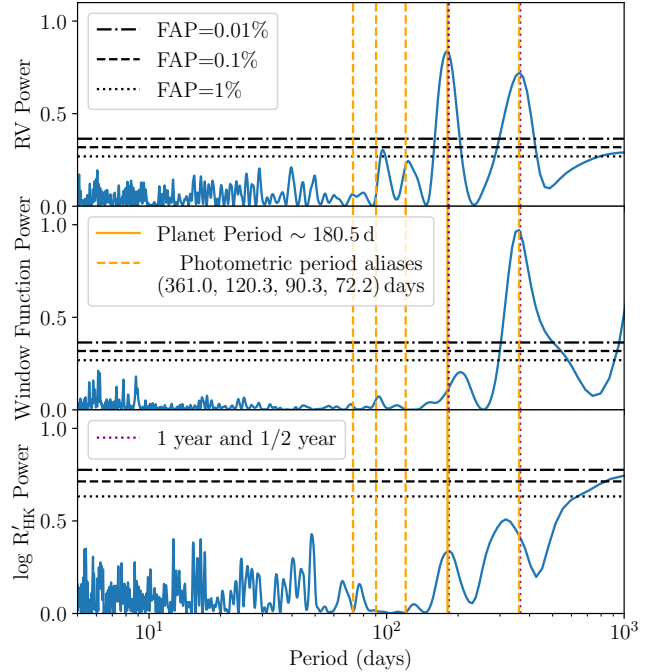


Figure 6. Spectroscopic Lomb-Scargle periodograms of the radial velocity timeseries (top), the combined HARPS and CORALIE window function (middle) and $\log R'_HK$ measurements from HARPS (bottom). The window function was created by running a Lomb-Scargle periodogram on the RV timeseries with a constant y value of 1. False alarm probabilities of 1%, 0.1% and 0.01% are represented by horizontal black lines with dotted, dashed and dash-dotted styles, respectively. A solid orange vertical line represents the orbital period of the planet at ~ 180.5 d while dashed vertical orange lines represent the photometric period aliases at 361.0, 120.3, 90.3 and 72.2 days. Additionally purple dotted vertical lines are shown to represent periods of 1 year and half a year.

tion 3.1) and the High Accuracy Radial velocity Planet Searcher (HARPS; Pepe et al. 2000; Mayor et al. 2003, Section 3.2). These spectra were used to produce time-series radial velocity measurements shown in Tables B1 and B2, respectively, and are presented together in Figure 5. Before any models were fitted to the data, we performed an initial search for periodic signals by creating a generalised Lomb-Scargle periodogram (Lomb 1976; Scargle 1982; Zechmeister & Kürster 2009) of the combined CORALIE and HARPS radial velocity data using ASTROPY (Astropy Collaboration et al. 2022). To combine these datasets we subtracted the median from each set of RVs before concatenating them together. The resulting periodogram is shown in Figure 6. The periodogram shows two peaks at ~ 180 and ~ 360 days which effectively rules out all but the 361 day and 180.5 day photometric period aliases (see Section 2). The relative strength of the 180.5 day peak compared to the 361 day signal as well as visually inspecting and comparing the best fits at both periods (see Figure 5a and Section 5) led us to conclude that the 180.5 day alias was in fact the true period of the system.

3.1 CORALIE

CORALIE is a fiber-fed echelle spectrograph with a resolution of $R \sim 60\,000$, mounted on the 1.2-m Leonhard Euler Telescope at ESO La Silla Observatory in Chile. CORALIE is capable of achieving radial velocity precision on the order of $\sim 10\,\text{m s}^{-1}$ (Queloz et al.

2001), which makes it well suited to the detection of giant planets such as NGTS-38 b.

On the night of 2023 April 16 a single spectrum of NGTS-38 was taken followed by an additional twelve points between 2023 December 10 and 2024 May 5, with a further 31 observations performed between 2024 October 21 and 2025 June 8 with 44 total spectra taken. All the observations of NGTS-38 taken with CORALIE had an exposure time of 1200-s and were taken at airmasses between 1.00 and 1.74 with the resulting spectra having signal-to-noise ratios (SNRs) between 19.6 and 40.4 in spectral order 62. The spectra were reduced using the standard CORALIE Data Reduction System (DRS) 3.8 with a G2 mask used for cross correlation that produced the radial velocity measurements shown in Table B1 and Figure 5. Due to an instrument update for CORALIE between the 2nd and 3rd set of observations described above, we treat the data from before and after this point as two separate instruments (CORALIE₁₄ and CORALIE₂₄, respectively) for the purpose of fitting instrumental offsets and jitter terms (see Section 5).

3.2 HARPS

Alongside the observations made with CORALIE, we also observed NGTS-38 with HARPS; a fiber-fed echelle spectrograph with a spectral resolution of $R \sim 115000$, which is mounted on the 3.6-m telescope at the ESO La Silla Observatory. The greater telescope diameter and spectral resolution of HARPS allow for more precise radial velocity measurements than CORALIE, with HARPS capable of reaching $\sim 1\text{m s}^{-1}$ precision.

The HARPS observations of NGTS-38 were taken in a very similar time-frame to the CORALIE data. Nine spectra were taken between 2023 December 20 and 2024 March 11, with a further 13 between 2024 October 14 and 2025 May 6. An additional HARPS spectrum, taken on 2026 January 5, was incorporated into the RV dataset but not used in the determination of the host star's spectral parameters (see Section 4.2). The first seven of these observations used an exposure time of 1500-s and were taken at airmasses between 1.02 and 1.59 with a resulting SNR of 51.4–78.4 in order 64. The remaining spectra were all taken with an exposure time of 1200-s at airmasses between 1.00 and 1.49 with resulting SNRs between 35.3 and 56.1 in order 64. These data were reduced with DRS 3.3.6 using an F9 mask. The resultant radial velocity values as well as activity indicators, including the S index derived $\log R'_{\text{HK}}$ value are shown in Table B2 and Figure 5.

4 HOST STAR ANALYSIS

4.1 Catalogue parameters

Catalogue parameters for TIC-65910228 / NGTS-38 are shown in Table 2. These were taken from the 2 Micron All Sky Survey (2MASS; Skrutskie et al. 2006), *Gaia* data release 3 (*Gaia* DR3; Gaia Collaboration et al. 2021), the *TESS* Input Catalogue v8 (TIC 8; Stassun et al. 2019), the AAVSO Photometric All Sky Survey (APASS; Henden & Munari 2014), the Wide field Infrared Survey Explorer (WISE; Wright et al. 2010), Tycho (Høg et al. 2000) and SkyMapper (Keller et al. 2007) Data Release 4 (DR4; Onken et al. 2024) catalogues where specified. We use the GAIADR3-ZEROPOINT package to calculate a zero point offset to the parallax as described in Lindegren (2020); Lindegren et al. (2021), finding a value of -0.01592 mas which we apply to the *Gaia* DR3 parallax of 3.7400 ± 0.0128 mas resulting in the final value we quote in Table 2.

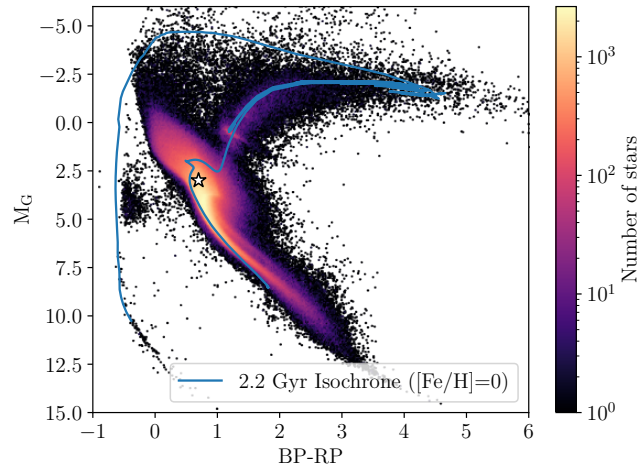


Figure 7. *Gaia* DR3 Hertzsprung-Russell diagram for all *TESS*-SPOC target stars from Doyle et al. (2024). NGTS-38 is overplotted as a white star with black borders. A solar metallicity 2.2 Gyr MIST isochrone (Dotter 2016; Choi et al. 2016) is overplotted as a solid blue line. The star sits significantly above the isochrone due to its enhanced metallicity giving it a larger radius (see Sections 4.3 and 6.1).

To aid in visualising the colour and magnitude information from these catalogues we overplot NGTS-38 on a *Gaia* DR3 Hertzsprung-Russell diagram (HRD; Hertzsprung 1913; Russell 1913) of all *TESS*-SPOC target stars from Doyle et al. (2024) in Figure 7. The star's position on the HRD shows a colour and luminosity broadly consistent with a main sequence F6-F7 type star, albeit a mildly over-luminous one.

4.2 Spectral fit

To fit spectral parameters for the host star we co-added the first 22 HARPS and 44 CORALIE spectra into two combined spectra with SNR values of 151 and 112, respectively.

We then analysed these spectra using Parameters Approximated With Synthesis (PAWS; Freckleton et al. 2024, 2025). PAWS uses the functions provided in the iSPEC package (Blanco-Cuaresma et al. 2014; Blanco-Cuaresma 2019) to determine the atmospheric parameters via the equivalent widths (EWs) of the Fe I and Fe II lines, assuming ionization and excitation equilibrium. The resulting values from this method were then used as priors for a spectral synthesis fit to obtain the final stellar parameters.

We calculated an inverse variance weighted mean of the results from both the CORALIE and HARPS spectra, obtaining values of T_{eff} , $[\text{Fe}/\text{H}]$, v_{mic} , v_{mac} , and $v \sin i_{\star}$ that we adopt in Table 2. Note that we do *not* adopt the spectroscopically derived $\log g$ of 3.8 ± 0.1 from PAWS as such values from spectra are known to be unreliable due to strong correlations with T_{eff} and $[\text{Fe}/\text{H}]$ (Torres et al. 2012; Mortier et al. 2014).

4.3 Isochrone fit

To determine the final set of stellar parameters we adopt in Table 2, we fitted the stellar models from the MESA (Modules for Experiments in Stellar Astrophysics; Paxton et al. 2010) Isochrones and Stellar Tracks (MIST; Dotter 2016; Choi et al. 2016) using the ISOCHRONES package (Morton 2015). In order to derive radius, mass (and thus

Table 2. NGTS-38 stellar parameters.

Property	Value	Source
<i>Identifiers</i>		
Tycho ID	6536-3043-1	Tycho (§4.1)
SkyMapper DR4 ID	35585731	SkyMapper (§4.1)
2MASS ID	J07145152-2925498	2MASS (§4.1)
Gaia Source ID	5606317297918628992	Gaia DR3 (§4.1)
TIC ID	65910228	TIC 8 (§4.1)
<i>Coordinates</i>		
RA (hh:mm:ss.ss)	07 : 14 : 51.52	Gaia DR3 (§4.1)
DEC (dd:mm:ss.ss)	-29 : 25 : 49.91	Gaia DR3 (§4.1)
<i>Proper motion and parallax</i>		
μ_{RA} (mas y^{-1})	13.5664 ± 0.0108	Gaia DR3 (§4.1)
μ_{DEC} (mas y^{-1})	-21.0834 ± 0.0131	Gaia DR3 (§4.1)
Parallax (mas)	3.75592 ± 0.01280	Gaia DR3 (§4.1)
Systemic velocity (km s^{-1})	19.9306 ± 0.0014	This work (§5)
<i>Galactic Kinematics</i>		
U (km s^{-1})	18.407 ± 0.096	This work (§4.5)
V (km s^{-1})	-32.8103 ± 0.054	This work (§4.5)
W (km s^{-1})	0.544 ± 0.019	This work (§4.5)
v_{tot} (km s^{-1})	37.62 ± 0.07	This work (§4.5)
e_{gal}	0.16	This work (§4.5)
J_z (kpc km s^{-1})	1608.6	This work (§4.5)
<i>Magnitudes</i>		
V (mag)	10.230 ± 0.020	APASS (§4.1)
B (mag)	10.738 ± 0.026	APASS (§4.1)
u (mag)	11.703 ± 0.011	SkyMapper (§4.1)
v (mag)	11.300 ± 0.011	SkyMapper (§4.1)
g (mag)	10.334 ± 0.009	SkyMapper (§4.1)
r (mag)	10.116 ± 0.010	SkyMapper (§4.1)
i (mag)	10.047 ± 0.017	SkyMapper (§4.1)
z (mag)	10.051 ± 0.012	SkyMapper (§4.1)
G (mag)	10.1103 ± 0.0002	Gaia DR3 (§4.1)
BP (mag)	10.3797 ± 0.0003	Gaia DR3 (§4.1)
RP (mag)	9.6821 ± 0.0002	Gaia DR3 (§4.1)
TESS (mag)	9.734 ± 0.006	TIC 8 (§4.1)
J (mag)	9.251 ± 0.026	2MASS (§4.1)
H (mag)	9.010 ± 0.026	2MASS (§4.1)
K (mag)	8.938 ± 0.023	2MASS (§4.1)
W1 (mag)	8.909 ± 0.023	WISE (§4.1)
W2 (mag)	8.947 ± 0.021	WISE (§4.1)
W3 (mag)	8.912 ± 0.027	WISE (§4.1)
<i>Spectral Parameters</i>		
v_{mic} (km s^{-1})	1.4 ± 0.2	This Work (§4.2)
v_{mac} (km s^{-1})	7.6 ± 0.8	This Work (§4.2)
$v \sin i_{\star}$ (km s^{-1})	12 ± 3	This Work (§4.2)
T_{eff} (K)	6310 ± 129	This Work (§4.2)
[Fe/H] ('dex')	0.33 ± 0.09	This Work (§4.2)
$\log g$ (log(cgs))	4.06 ± 0.02	This Work (§4.3)
$\log R'_{\text{HK}}$	-5.07 ± 0.07	This Work (§4.4.2)
<i>Derived parameters</i>		
ρ_{\star} (g cm^{-3})	$0.302^{+0.035}_{-0.030}$	This Work (§5)
R_{\star} (R_{\odot})	1.88 ± 0.08	This Work (§4.3)
M_{\star} (M_{\odot})	1.46 ± 0.09	This Work (§4.3)
Age (Gyr)	2.2 ± 0.5	This Work (§4.3)
Distance (pc)	265 ± 1	This Work (§4.3)

isochronal $\log g$), and age, we used the optical B and V band magnitudes as well as the J,H,K,W1,W2 and W3 magnitudes to cover a wider range of the spectral energy distribution. All of these magnitudes are listed in Table 2. We furthermore used the values of T_{eff} and [Fe/H] from PAWS (see Section 4.2) and the zero point corrected *Gaia* DR3 parallax applied listed in Table 2. Finally, we also used the host density ($0.302^{+0.035}_{-0.030}$ g cm^{-3}) derived from preliminary fits to the transit data with no stellar parameters inputted (see Section 5). We note that the final result did not depend, within errors, on the inclusion or exclusion of the stellar density derived from the transit. Final values and precision uncertainties were extracted as the median value and the 16th and 84th percentiles of the posterior distributions.

We adopt the recommendations of Tayar et al. (2022) to account for the inherent uncertainties between stellar models; adding an additional 0.042% error term in quadrature to the host radius. In addition we made use of the KIAUHOKU package (Claytor et al. 2020) to compare fits of the spectroscopic T_{eff} , $\log g$ and [Fe/H] against MIST, Dartmouth (Dotter et al. 2008), Yale Rotating stellar Evolution Code (YREC; Demarque et al. 2008) and Garching STellar Evolution Code (GARSTEC; Weiss & Schlattl 2008) stellar models. We calculated the standard deviation across the values fitted against each model and added these in quadrature to our values. This error term for $\log g$ was so small as to be negligible ($\sim 10^{-7}$). However, we used terms for the stellar mass and age of $0.08 M_{\odot}$ and 0.4 Gyr, respectively. With these error terms added this resulted in the final stellar parameters we adopt in Table 2.

4.4 Activity and rotation

4.4.1 Rotation

Using equation 1 from Watson et al. (2010) and our value of $v \sin i_{\star}$ from PAWS (see Section 4.2), we estimate an upper limit on the stellar rotation period of 8 ± 2 d. We attempt to measure a photometric rotation period by creating Lomb-Scargle periodograms on the largest consecutive runs of each of our datasets. For NGTS we use the first run between 2023 August 25 - 2024 February 4 and for *TESS* we separately median normalised and then stitched together the SPOC lightcurves (using the SAP_FLUX column) for sectors 87 and 88. We also used the entire WASP and ASAS-SN datasets (See Section 2.4.1 and 2.4.2), separating the latter by V and g bands. The resulting periodograms are shown in Figure 8.

The *TESS* periodogram shows two peaks of interest, one at 6.7 d and another broad peak around $\sim 20 - 30$ d. However, these are close to the mid orbit gap and mid sector gap, respectively, and should be interpreted cautiously. The NGTS periodogram is noisier than *TESS* but still shows a few peaks of interest. The peak at ~ 1 d is almost certainly due to the nightly cadence of the data. There is a peak at 6.9 d similar to that found in *TESS*, with another at 26.9 d which coincides with the lunar period of 27.3 d and thus is likely caused by dilution from moonlight modulating with the lunar phases. Another peak appears at 93 d, however given this is approaching the baseline it should also be interpreted cautiously. A peak at ~ 7 d appears in both *TESS* and NGTS photometry and is in agreement with the $v \sin i_{\star}$ derived rotation period – lending some credence that this may be the true rotation period of the star. However, phase folding on this period doesn't show a clear sinusoidal signal for either dataset. Additionally, we do not see this peak in either ASAS-SN bandpass, seeing only a ~ 300 d peak in both likely due to the Earth's orbit and another at 29.5 d in the g band likely due to the moon. The WASP periodogram also shows no convincing peaks at any period beyond ~ 1 d. Hence

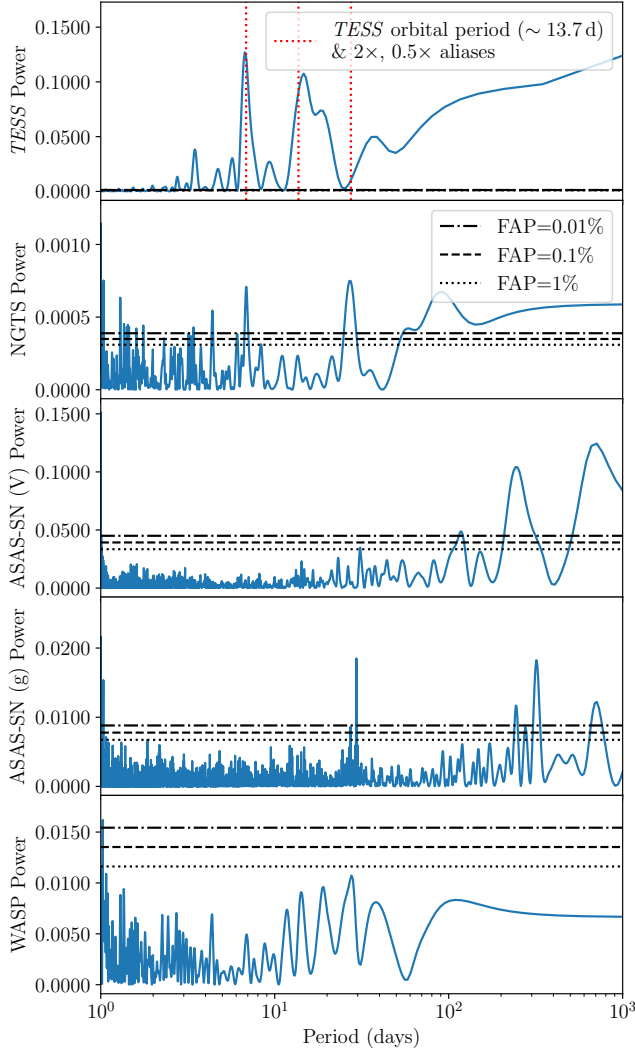


Figure 8. Lomb Scargle periodograms of *TESS* sectors 87 and 88 (top), the first run of NGTS data (upper middle), ASAS-SN in both the V band (middle) and g band (lower middle) and WASP (bottom) for NGTS-38. False alarm probabilities of 1%, 0.1% and 0.01% are represented by horizontal black lines with dotted, dashed and dash-dotted styles respectively. For *TESS*, its 13.7 d orbital period is marked with a vertical red dashed line as well as aliases at $2\times$ (a *TESS* sector duration) and $0.5\times$ this period (which coincides with the mid-orbit gap in newer sectors).

we conclude that, in spite of a tentative ~ 7 d signal, we do not recover any significant rotation period for NGTS-38 photometrically.

4.4.2 $\log R'_{\text{HK}}$

We calculated an inverse variance weighted mean and standard deviation of all the individual values of $\log R'_{\text{HK}}$ calculated by the DRS from each HARPS spectrum (see Table B2), finding of $\log R'_{\text{HK}} = -5.07 \pm 0.07$. This indicates a low level of stellar activity, albeit not unusually so for an F6-F7 star (See $\log R'_{\text{HK}}$ catalogues; Jenkins et al. 2006, 2008, 2011).

A potential long-term downward trend in $\log R'_{\text{HK}}$ is visible. This trend is, however, unlikely to be genuine as the lower $\log R'_{\text{HK}}$ data points have systematically poorer precision and come from lower signal to noise spectra. We still attempted to investigate this by pro-

ducing a periodogram of the $\log R'_{\text{HK}}$ data, which we present in Figure 6. The periodogram shows a potential long term trend with a high plateau in power beyond 10^3 d, although this could be driven by the lower SNR spectra taken later in the campaign. Also notable are the peaks that appear to coincide with those in the RV periodogram at ~ 180 and ~ 360 . There is also a weak negative correlation between the RVs and $\log R'_{\text{HK}}$. Although, it is highly unlikely that the RV signal is activity induced due to its high amplitude. These peaks are instead likely an artefact of the spectroscopic window function. This is further supported by the fact that we see no similar peaks or RV correlations in other activity indicators such as the Full Width Half Maximum (FWHM) and Bisector Inverse Slope (BIS).

4.5 Galactic Kinematics and population membership

Using the proper motions and parallax reported in Gaia DR3 and the HARPS systemic RV (see Sections 3.5 and Table 2), we compute the kinematic properties of NGTS-38 following Johnson & Soderblom (1987); Bensby et al. (2003) and report U, V and W in Table 2. As laid out in Bensby et al. (2003, 2014); Reddy et al. (2006), we compute the kinematic membership probability by correcting for the Local Standards of Rest reported in Koval' et al. (2009); Schönrich et al. (2010); Coşkunoğlu et al. (2011); Bobylev & Bajkova (2014); Francis & Anderson (2014); Tian et al. (2015) and Almeida-Fernandes & Rocha-Pinto (2018), also using the velocity dispersions and stellar fractions reported in Bensby et al. (2014); Chen et al. (2021). This results in a weighted kinematic thin disc probability of 98.2% for NGTS-38. This is consistent with the star's enriched metallicity as thin disc stars are typically more metal rich than those in the thick disc (Bensby et al. 2003, 2014).

5 ORBITAL SOLUTION

We performed a joint model fit to the combined photometric and spectroscopic radial velocity dataset using the ALLESFITTER package (Günther & Daylan 2019, 2021), which packages together various fitting code suites with the ELLC modelling package (Maxted 2016). We opted to use nested sampling (Skilling 2004; Skilling 2006) via the DYNESTY package (Speagle 2020) contained within ALLESFITTER.

ALLESFITTER uses 8 main fitted astrophysical parameters to describe the orbital solution of a system. The first and simplest of these is the orbital period, P , in days. Transit timings are described largely by this as well as the transit epoch, T_0 . The transit shape comes from the radius ratio between the planet and host star, R_p/R_\star , the combined host and planet radius relative to the orbital semi-major axis, $(R_\star + R_p)/a$, and the cosine of the orbital inclination, $\cos i$. Radial velocity data solely determines the semi-amplitude, K , in km s^{-1} and also largely controls the orbital eccentricity (e) and angular argument of periastron (ω), parametrized as $\sqrt{e} \sin \omega$ and $\sqrt{e} \cos \omega$.

On top of these astrophysical parameters, a wide array of instrumental parameters were also fitted to the data. For photometry we included logarithmic error terms, $\log \sigma$ per instrument, which we initially set with wide uniform priors between -14 and 0. For all ground based photometry instruments we fit a simple flux baseline offset term with a uniform prior between ± 0.001 . For *TESS* we performed a least squares minimisation spline fit to the baseline at each sampling step using ALLESFITTER's built in `hyrbid_spline` method. We modelled limb darkening using a quadratic law, for which ALLESFITTER uses the q_1, q_2 parametrization from Kipping (2013), varying the priors between 0 and 1 for all instruments in all fits with the exception of the final fit described later in this section. The limb-darkening

parameters were coupled together for the four LCOGT instruments. For the radial velocity data, a logarithmic jitter term, $\log \sigma$, was fitted per instrument with initial uniform priors, as well as an RV baseline offset.

The first fit we performed was only to the *TESS* and radial velocity data. We allowed the period to vary uniformly between 179 and 181 days, based on the most likely peak in the RV periodogram (see Figure 6). Similarly, the transit epoch had a uniform prior distribution of a 2 day range centred on the reported *TESS* epoch on BJD=2459209.228. Wide uniform priors of $\mathcal{U}(0, 0.1)$, $\mathcal{U}(0, 0.05)$ were placed on R_p/R_\star and $(R_\star + R_p)/a$, respectively, based on visual inspection of the *TESS* transit. The radial velocity semi-amplitude was allowed to vary between 0 and 500 m s^{-1} . $\cos i$ was allowed to vary across its full possible range between 0 and 1 and the parameters of $\sqrt{e} \sin \omega$ and $\sqrt{e} \cos \omega$ were similarly sampled across their full possible ranges between -1 and 1. The RV baseline priors were set between 19.95 and 20.05 km s^{-1} for both CORALIE epochs and between 19.9 and 20 km s^{-1} for HARPS, in both cases based on a visual inspection of the data. All RV instrumental jitter terms had uniform priors between -7.6 and $-4.6 \ln \text{km s}^{-1}$. The transit parameters resulting from this fit were used for the template matching used to detect the NGTS egress described in Section 2.2.

After the detection of the NGTS egress (see Section 2.2), the detrended NGTS lightcurve was incorporated into a fit. The period of $180.531 \pm 0.001 \text{ d}$ and epoch of $\text{BJD} = 2459209.2277 \pm 0.0032$ from this fit were used to schedule the simultaneous set of additional transit observations described in Section 2.3.

We performed one final preliminary on the data incorporated the entire dataset and was performed to determine the transit derived stellar density used in the host star characterisation (see Section 4.3). As with all the previous fits, no stellar parameters were inputted to ALLESFITTER to avoid any biasing of the resulting stellar density value. In addition we conducted a second fit with the same setup except the period prior distribution was uniform between 360 and 362 days instead of 179 and 181 days. Whilst the $\mathcal{U}(179, 181)$ day period prior fit provided a good fit to the data, the $\mathcal{U}(360, 361)$ day fit was much poorer (see Figure 5a), effectively allowing us to rule out this period.

The final fit was largely identical to the penultimate fit except for the addition of the stellar radius, mass and effective temperature into the fit, which allowed the determination of derived parameters such as the planet mass and radius. We also allowed ALLESFITTER to use these stellar parameters to set an external prior on the stellar density. Solutions where the derived host density did not match this prior were penalised. In addition, we used the Limb Darkening Tool Kit (LDTK; Parviainen & Aigrain 2015) package to determine priors on the limb darkening coefficients. Since, LDTK returns limb darkening coefficients in the usual u_1, u_2 parametrization, we converted these values back to the Kipping (2013) q_1, q_2 parameters in order to be usable in ALLESFITTER. LDTK uses values of the host star T_{eff} , $[\text{Fe}/\text{H}]$ and $\log g$ along with filter response functions for each instrument. For *TESS*, NGTS and LCOGT exact filter response functions were available while for the El Sauce, DSC0.4m and OACC-CAO instruments we used generic Cousins R, Johnson R, and Sloan i' filters respectively from the Spanish Virtual Observatory filter profile service,³ assuming these to be close enough approximations. In these cases we widened the spread of the normal priors on both limb darkening coefficients by a factor of 3 to account for the approximation.

The prior and posterior distributions of all parameters in this fit

Table 3. NGTS-38 b properties

Parameter	Value	Source
Period (days)	180.52791 ± 0.00038	ALLESFITTER
<i>Transit Parameters</i>		
T_0 (BJD)	2459209.2286 ± 0.0031	ALLESFITTER
R_p/R_\star	0.05909 ± 0.00061	ALLESFITTER
R_\star/a	0.01258 ± 0.00035	ALLESFITTER
b_{transit}	$0.8540^{+0.0090}_{-0.010}$	ALLESFITTER
$b_{\text{occultation}}$	0.59 ± 0.03	This work (§7.2)
T_{14} (hrs)	14.88 ± 0.13	ALLESFITTER
T_{23} (hrs)	$9.38^{+0.27}_{-0.29}$	ALLESFITTER
<i>RV parameters</i>		
K (km s^{-1})	0.1372 ± 0.0018	ALLESFITTER
e	0.308 ± 0.011	ALLESFITTER
ω (degrees)	278.11 ± 0.70	ALLESFITTER
<i>Derived parameters</i>		
R_p (R_J)	1.081 ± 0.047	ALLESFITTER
M_p (M_J)	$4.78^{+0.40}_{-0.37}$	ALLESFITTER
ρ_p (g cm^{-3})	$4.69^{+0.95}_{-0.78}$	ALLESFITTER
$\log g$ ($\log(\text{cgs})$)	3.98 ± 0.03	ALLESFITTER
a (au)	0.695 ± 0.036	ALLESFITTER
Periaxis (au)	0.481 ± 0.026	$a(1 - e)$
Apoapsis (au)	0.91 ± 0.05	$a(1 + e)$
T_{eq} (K)	458 ± 11	ALLESFITTER
$T_{\text{eq:Apoa}}$ (K)	400 ± 10	This work (§6.1)
$T_{\text{eq:Peria}}$ (K)	550 ± 14	This work (§6.1)
R_{Hill} (R_J)	147 ± 9	This work (§7.4)
d_{Roche} (R_J)	3.50 ± 0.28	This work (§7.4)

are shown in Table C1. Also presented are the derived parameters using the inputted stellar parameters, shown in Table C2.

6 RESULTS

6.1 The TIC-65910228/NGTS-38 system

TIC-65910228/NGTS-38 is a bright ($\text{Vmag}=10.230 \pm 0.020$) star with a temperature of $6310 \pm 129 \text{ K}$, which is consistent with an F6V-F7V type star (Pecaut & Mamajek 2013). While the star may superficially appear evolved due to its large radius ($1.88 \pm 0.08 R_\odot$) compared to its mass ($1.46 \pm 0.09 M_\odot$) and resulting low surface gravity ($\log g=4.06 \pm 0.02$), the star is still on the main sequence. In evolutionary models of F type stars (e.g. Dotter 2016; Choi et al. 2016), the stellar radius is fairly dependent on metallicity as a higher metallicity leads to higher opacities in the upper stellar atmosphere. Hence, a metal rich star like NGTS-38 ($[\text{Fe}/\text{H}]=0.33 \pm 0.09$) can have an apparently inflated radius before leaving the main sequence (See the isochrone in Figure 7). This is reflected in the isochrone derived stellar age of $2.2 \pm 0.5 \text{ Gyr}$ we find for NGTS-38, which is expected of an F6-F7 type star on the main sequence.

The system is host to a transiting planet companion, NGTS-38 b, for which we list some properties in Table 3. We find the planet to have a radius similar to that of Jupiter ($R_p=1.081 \pm 0.047 R_J$) but almost five times the mass ($M_p=4.78^{+0.40}_{-0.37} M_J$), placing it firmly among the rare ‘super-Jupiter’ class of exoplanets. The planet is on a long-period ($P=180.52791 \pm 0.00038 \text{ d}$), wide separation ($a = 0.695 \pm 0.036 \text{ au}$) orbit with a moderate eccentricity ($e = 0.308 \pm 0.011$). Its wide orbital separation gives NGTS-38 b a relatively cool equilibrium tempera-

³ Available at <https://svo2.cab.inta-csic.es/theory/fps/>

ture for a transiting exoplanet with $T_{\text{eq}}=458 \pm 11$ K at its semi-major axis. It should be noted, however, that a planet with as long a period and as eccentric an orbit as NGTS-38 b will experience temperature fluctuations throughout its orbit. Using the same assumptions used by ALLESFITTER to estimate T_{eq} at a (those being a Jupiter like albedo of 0.3 and emissivity of 1) we calculate the equilibrium temperature at periastron and apastron, which we list in Table 3.

6.1.1 Tidal interactions

For a planet as distant from its host as NGTS-38 b, tidal interactions are expected to be negligible. To test this, we first calculate the tidal circularisation timescale using equation 4 from Jackson et al. (2008). We use a range of values for the planetary tidal quality factor $10^4 \leq Q_P \leq 10^7$. All the resulting timescales are between $\sim 10^5 - 10^8$ Gyr, more than the current age of the universe and far longer than both the current age and expected lifespan of the host star. As such we conclude that the planet's eccentricity has not been significantly damped by tidal interactions with the host star in its lifetime and the planet will not experience any significant damping of its eccentricity until the host star begins post main sequence evolution.

An accurate tidal locking timescale for a non-rigid body such as NGTS-38 b is a more complex affair (see; Dewberry 2024) and beyond the scope of this paper. However, we can obtain a reasonable estimate using equation 1 from (Guillot et al. 1996) assuming an initial rotation rate equal to that of Jupiter ($\omega_P = 1.7 \times 10^{-4} \text{ s}^{-1}$) and varying Q_P again between 10^4 and 10^7 . The resulting values are on the order of 10^{60} Gyr, essentially meaning the planet will never be tidally locked during the host star's main sequence lifetime.

6.2 NGTS-38 b in a population context

NGTS-38 b is one of the longest period transiting planets ever discovered being in the 97.5th percentile of all transiting planets in terms of orbital period (NASA exoplanet archive; Akeson et al. 2013; Christiansen et al. 2025). Within this 97.5th period percentile it is also one of the most amenable to characterisation with its host star belonging to the 90th percentile in V band magnitude. NGTS-38 b is also one of only thirteen planets with orbital periods > 100 d to be discovered by the *TESS* mission at the time of writing, being the 7th longest period of these.

The mass of NGTS-38 b is just within the sparsely populated mass regime between $\sim 4 M_J$ and $\sim 10 M_J$, proposed to represent the transition from core accretion to gravitational instability as the primary mechanism of planet formation (Santos et al. 2017; Schlaufman 2018; Narang et al. 2018). NGTS-38 b's presence in this mass regime may be more intriguing given the enriched metallicity of its host star since Narang et al. (2018) find the occurrence rate of planets with $M_p \geq 4 M_J$ decreases with increasing host metallicity (although the occurrence of planets with periods longer than 10 days increases). Additionally the moderate eccentricity of NGTS-38 b ($e=0.308 \pm 0.011$) is consistent with the peak in the eccentricity of super-Jupiters at $e \sim 0.3$ identified by Blunt et al. (2026).

6.2.1 Archive sample

We retrieved a sample of transiting exoplanets with well defined parameters from the NASA exoplanet archive on 2026/01/16 to compare against NGTS-38 b. We used the planetary systems composite data table, containing 6071 entries, to avoid repeated entries of the

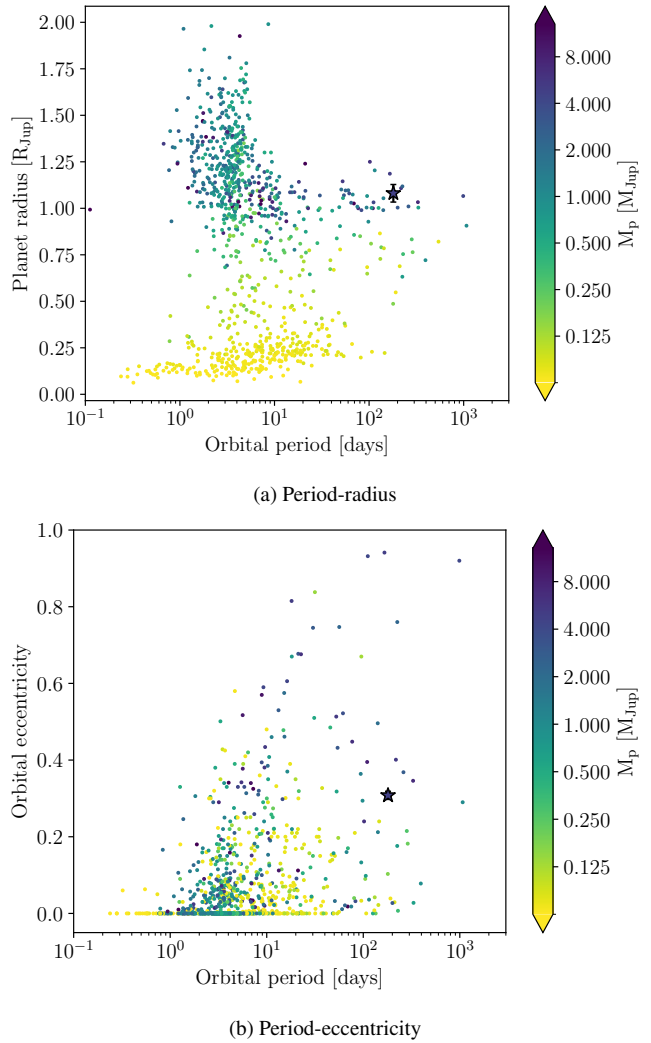


Figure 9. Exoplanet population plots with NGTS-38 b overplotted as a black-bordered star. Orbital period on a base 10 logarithmic scale is plotted against planet radius (top) and eccentricity (bottom). The exoplanet population used is described in §6.2.1. Points on all of the plots are coloured by mass.

same planet. First we eliminated dubious planets by setting the controversial flag to 0 and limited our sample to only transiting planets by setting the detected by transits flag to 1. We then similarly set the limit flags on radius, mass (eliminating $M_{\text{sin } i}$ only constraints) and orbital periods to 0 to only allow constrained values on these parameters. We also only allowed systems with a constrained mass rather than $M_{\text{sin } i}$. This left us with 1434 planets. We then made a precision cut of 25% on mass, 10% on radius and 1% on orbital period, leaving 939 planets in the final comparison sample. We show NGTS-38 b plotted with this sample in Figure 9. Of these, NGTS-38 b has the 16th longest period.

6.3 Interior

As can be seen in Figure 10, NGTS-38 b appears to have a normal radius and density for a temperate planet of its mass, unaffected by inflation like many hotter planets.

We used the planetary code COMPLETO (Mordasini et al. 2012) to estimate the heavy element content of NGTS-38 b. We built a grid of interior models assuming that planets are described with a

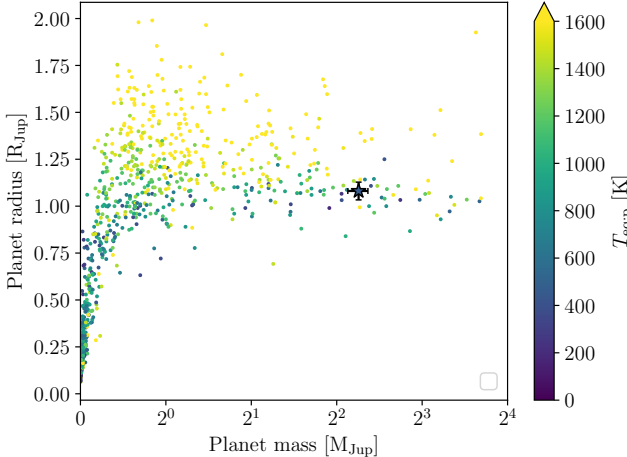


Figure 10. Planet mass in Jupiter masses (on a \log_2 scale) plotted against planet radius in Jupiter radii for the transiting planet population described in §6.2.1. Planets are coloured by their equilibrium temperature. NGTS-38 b is shown as a black bordered star with errorbars. The red dashed line shows a mass-radius relation created using GASTLI (Acuña et al. 2021, 2024) for a planet with a core mass fraction of 0 and a pure solar envelope composition with the equilibrium and internal temperatures set to 500 K and 100 K, respectively.

layered model including a core with a mass comprised between 0 and $10 M_{\oplus}$ and an envelope coupled with a semi-grey atmospheric model. The heavy elements are modelled as water with the AQUA equation of state (EoS) from Haldemann et al. (2020) and they are homogeneously mixed in the H/He envelope are described with EoS from Chabrier & Debras (2021).

The grid of evolution models was then coupled to a Bayesian inference model to retrieve the heavy element content that is compatible with the observed planetary mass, radius, equilibrium temperature, and age of the system. We find that the heavy element mass (M_Z) is equal to $110^{+90}_{-80} M_{\oplus}$. The overall stellar metallicity is approximated with a scaling law with the iron abundance $Z_{\star} = 0.0142 \times 10^{[\text{Fe}/\text{H}]}$ (Asplund et al. 2009). The planetary heavy element enrichment (Z_p/Z_{\star} , with $Z_p = M_Z/M_p$) is equal to $2.4^{+2.0}_{-1.7}$. This value is consistent with no metal enrichment of NGTS-38 b relative to its host star at 2σ . This result is in line with other high-mass ($M > 2 M_{\oplus}$) and weakly irradiated giant planets orbiting metal-rich stars, such as Kepler-1704 b (Dalba et al. 2021) or TOI-2180 b (Dalba et al. 2022), which also show relatively low bulk metal enrichment. We note that the results of the interior structure modelling are dependent on several assumptions, in particular regarding the chosen interior structure and equations of state. The planetary metal enrichment can vary depending on these model assumptions but also on the interior modelling codes used to explore the planet’s composition.

7 DISCUSSION

7.1 Alignment

We do not find a photometric rotation period for TIC-65910228 / NGTS-38 to compare against the spectroscopic $v \sin i_{\star}$ derived upper limit (see Section 4.4.1). This makes any constraints on the alignment of NGTS-38 b impossible without measuring the sky projected obliquity by observing the Rossiter-McLaughlin effect via a spectroscopic transit. If this was done, it would make NGTS-38 b the third

longest period planet with a measured obliquity behind HIP 41378 d and f (Grouffal et al. 2022, 2025) and one of only five such systems with periods beyond 100 d. The planet’s moderate eccentricity would also make it stand out among this sample, with the other four systems having either effectively circular or highly eccentric orbits (Source: NASA exoplanet archive; Akeson et al. 2013; Christiansen et al. 2025, Accessed 2026/01/16). Of additional interest, is the fact that the effective temperature of the host star lies close to the Kraft break (Kraft 1967), which has been linked to a bimodal distribution in observed giant planet obliquities (Winn et al. 2010; Albrecht et al. 2012b; Winn & Fabrycky 2015; Triaud 2018; Albrecht et al. 2022; Knudstrup et al. 2024; Wang et al. 2024).

Using equation 1 from Triaud (2018) we estimate an RM amplitude of $14 \pm 3 \text{ m s}^{-1}$ for NGTS-38 b. This is within the detection limits of high precision radial velocity spectrographs such as the Echelle SPectrograph for Rocky Exoplanets and Stable Spectroscopic Observations (ESPRESSO, Pepe et al. 2021) and potentially HARPS, albeit marginally. Although, the long transit duration ($T_{14} = 14.88 \pm 0.13$ hrs) of NGTS-38 b will make such observations challenging from the ground. However, using multiple facilities across the globe it may be possible to obtain an effective observation baseline long enough to view the entire spectroscopic transit. This approach has already been effectively used for RM observations of the long-period planets in the HIP 41378 system (Grouffal et al. 2022, 2025).

7.2 Atmosphere

As can be seen in Figure 11, NGTS-38 b has one of the coolest equilibrium temperatures out of our sample of transiting exoplanets with well defined parameters (see Section 6.2.1). The equilibrium temperature of 458 ± 11 K is below the 500 K N_2 to NH_3 transition line (Fortney et al. 2020) where the atmospheric nitrogen content switches between being dominated by diatomic Nitrogen to more complex molecular species. The planet’s host star also has one of the hottest effective temperatures of any planet with a temperature near-to / below this transition line, potentially leading to unique photochemistry in the upper atmosphere. Although, it should be noted that the equilibrium temperature at periastron (550 ± 14 K) is above this transition. It is also important to note that the chemical transition temperatures we quote from Fortney et al. (2020) are calculated for a $1 M_{\oplus}$ planet as this is the closest to the mass of NGTS-38 b of the three masses Fortney et al. (2020) calculate transition temperatures for. Fortney et al. (2020) note that the temperatures at which these transitions occur are also dependent on surface gravity, pressure and mixing ratios among other factors with a more massive planet like NGTS-38 b potentially seeing these transitions occur at higher temperatures. For a $10 M_{\oplus}$ planet the N_2 to NH_3 transition could instead occur at ~ 550 K instead of ~ 500 K for a $1 M_{\oplus}$ planet.

In addition, the wide orbital separation of the planet means the rotation is unlikely to be tidally locked (see Section 6.1.1). The lack of a permanent day or night side will almost certainly have significant effects on the heat distribution and circulation dynamics of the planet. Similarly, the lack of tidal locking means the planetary rotation period could be much shorter than most hot-Jupiters, leading to further differences in atmospheric dynamics. For reviews into the atmospheric dynamics of giant planets, including rotational and tidal locking effects see: Pierrehumbert & Hammond (2019) and Showman et al. (2020).

To test the observability of NGTS-38 b’s atmosphere, we calculate the Transmission Spectroscopy Metric (TSM; Kempton et al. 2018) for NGTS-38 b, finding a low value of ~ 2.1 . The planet’s high mass

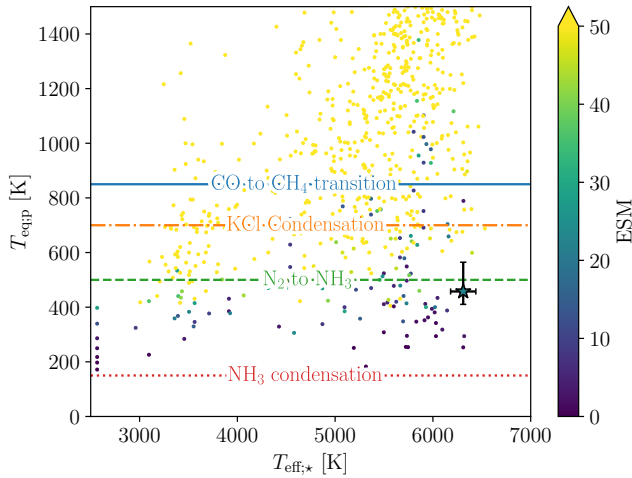


Figure 11. Stellar effective temperature, T_{eff} , plotted against planetary equilibrium temperature, T_{eq} , for a sample of transiting planet systems described in §6.2.1. NGTS-38 b is overplotted as a black bordered star with errorbars sized to reflect the range of equilibrium temperatures throughout the planet’s orbit. Points are coloured according to their Emission Spectroscopy Metric (ESM; Kempton et al. 2018). Horizontal lines are plotted at 850, 700, 500 and 150 K to indicate the CO to CH₄ transition, KCl condensation, the N₂ to NH₃ transition and NH₃ condensation, respectively, for a 1M_J planet (Fortney et al. 2020).

results in a low atmospheric scale height and thus lower signal-to-noise compared to a less massive planet. This makes the planet a poor prospect for transmission spectroscopy follow-up.

Because emission SNR is largely independent of planet mass we also investigate emission spectroscopy as an alternative approach to probing the planet’s atmosphere. Given the planet’s large orbital separation and relatively high transit impact parameter ($b_{\text{transit}}=0.8540^{+0.0090}_{-0.010}$) a secondary eclipse would seem relatively unlikely. However, using equation 8 from Winn (2014), we find a value of $b_{\text{occultation}}=0.59 \pm 0.03$, meaning the planet is occulted by its host and emission spectroscopy may be possible. We calculate a value of the Emission Spectroscopy Metric (ESM; Kempton et al. 2018) - although we choose to use the equilibrium temperature for NGTS-38 b instead of estimating a daytime temperature, since the planet is extremely unlikely to be tidally locked at its wide orbital separation. Using this method we find a value of ~ 22.5 , which, while modest, is relatively high for a planet with as low an equilibrium temperature as NGTS-38 b (see Figure 11).

7.3 Additional planetary companions

Multiplicity is common in exoplanetary systems with 2574 out of 6071 ($\sim 42\%$) confirmed planets being in systems with other planets (Source: NASA exoplanet archive; Akeson et al. 2013; Christiansen et al. 2025, Accessed 2026/01/16). A number of transiting warm Jupiter systems have already been found to host smaller inner companions (e.g. NGTS-11 b and c; Gill et al. 2020c; Anderson et al. 2025) and warm-Jupiters appear to be more likely to have close planetary neighbours than their hot-Jupiter counterparts (Huang et al. 2016). Given the wide orbital separation of NGTS-38 b it is fairly likely that additional interior planets could have stable orbits. With this in mind we performed a transit least squares search on the *TESS* dataset using the *ALLESFITTER* package which acts as a wrapper for the *TRANSITLEASTSQUARES* package (Hippke & Heller 2019) along-

side *WOTAN* (Hippke et al. 2019) for detrending. However, this search returned no convincing results. Additionally a generalised Lomb-Scargle periodogram of the RV residuals showed no significant peaks. Thus we detect no additional companions apart from NGTS-38 b, although this does not necessarily rule out the existence of any other companions in the system.

7.3.1 Sensitivity maps

To ascertain the detection limits of the *TESS* data for NGTS-38 we made use of the Transit Investigation and Recoverability Application (TIARA; Rodel et al. 2024). TIARA takes photometric data as inputs, specifically lightcurve timestamps, contamination values and measured photometric precision with the latter two in this instance being taken from the lightcurve *fits* file headers 1-CROWDSAP and CDPP2_0, respectively. The sector 61 lightcurve lacked a recorded noise value so we instead used the sector 34 noise value in its place. TIARA then uses the lightcurve properties to calculate the signal-to-noise and detection probability of generated signals producing a sensitivity map which we show with a smoothing function from Eschen et al. (2024) in Figure 12a. The resulting sensitivity map shows that planets smaller than 2-4 R_⊕ (depending on orbital period) are unlikely to be detectable in the *TESS* data, at least at periods shorter than ~ 100 days. This allows us to effectively rule out larger transiting companions than this, although, the aforementioned lack of any residual RV signal makes any large non-transiting companions additionally unlikely.

Potential small inner transiting companions around NGTS-38 could be detected with the upcoming PLAnetary Transits and Oscillations of Stars (*PLATO*; Rauer et al. 2025) mission. This mission will observe a field spanning $\sim 5\%$ of the sky. For at least the first two years of its mission, *PLATO* will observe a field in the Southern Hemisphere, LOPS2 (Nascimbeni et al. 2025). Unlike *TESS* which observes a target with one of its four cameras, *PLATO* has four sets of six cameras that overlap in the centre of its field. Hence a target can be observed with 6, 12, 18 or 24 cameras resulting in a higher precision of the photometric data. This and its longer observations enable *PLATO* to detect planets smaller than *TESS* (Rauer et al. 2025; Eschen et al. 2024). NGTS-38 lies within the *PLATO* LOPS2 field and will be monitored by *PLATO* with 6 cameras during its observation of the Southern field. These observations will not only enable us to determine the period and ephemeris more precisely but also to search for smaller inner companions. Following Eschen et al. (2024), we apply TIARA to 2 years of simulated *PLATO* data using the noise (Börner et al. 2024) reported in the *PLATO* Input Catalogue (Montalto et al. 2021). These simulations show that *PLATO* is predicted to detect potential inner companions down to sub 1 R_⊕ radii at short periods as we show in Figure 12b.

7.4 Potential for the detection of exomoons and exorings

We find no observational evidence of exomoons or exorings around NGTS-38 b. However, its large mass and wide orbital separation make it a potentially high value target in future searches for such circumplanetary systems. In the remainder of this section we assess the ability of the planet to form and retain moons and/or rings and the potential to detect them.

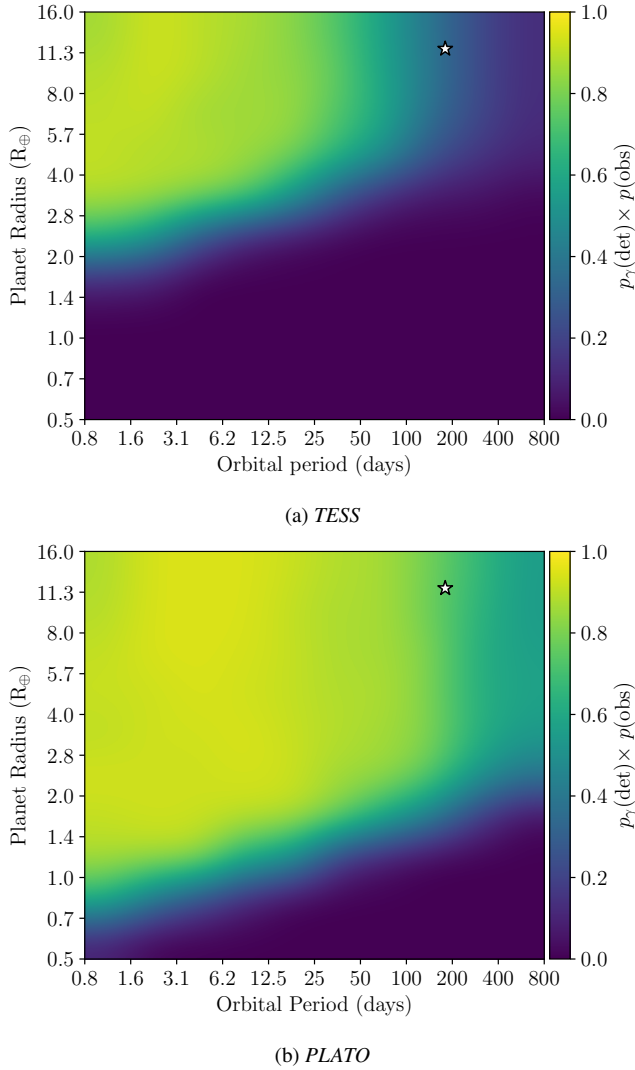


Figure 12. TIARA sensitivity maps for NGTS-38 in *TESS* (top) and *PLATO* (bottom) with NGTS-38 b overplotted as a white star with black borders.

7.4.1 Formation and retention

The planet's current position is well interior to any primordial ice line of the system making the formation of icy moons or rings like those in the solar system unlikely if the planet formed in situ. If the planet formed beyond the ice line and migrated inwards any icy moons or rings would have to survive this migration. The theoretical lifespans of rings are too short to allow survival of such a ring system to the present. Moons could potentially survive such a migration, although dynamically violent migration mechanisms could potentially be more likely to disrupt any moons present (Gong et al. 2013). Alternatively, moons or rings could be formed from the volatile poor silicate material found in the inner region of the disk.

Barnes & O'Brien (2002) find no meaningful upper limit on the mass of moons able to survive for planets orbiting their hosts beyond ~ 0.6 au. NGTS-38 b sits on the edge of this limit with its semi major axis of 0.695 ± 0.036 au, although its moderate eccentricity means the periastron distance falls below this limit. However, based on figure 2 of Barnes & O'Brien (2002) this still allows the survivability of a $\approx 1 M_{\oplus}$ satellite.

To further investigate the survivability and possible extent of

circumplanetary systems around NGTS-38 b, we calculate the Hill sphere radius as follows:

$$R_{\text{Hill}} = a \sqrt{\frac{M_p}{3(M_p + M_{\star})}}, \quad (1)$$

finding a value of $147 \pm 9 R_J$. This is much smaller than that of Jupiter ($\sim 700 R_J$) but still relatively large compared to most transiting exoplanets. Rosario-Franco et al. (2020) find that moons are stable out to $\lesssim 0.3 R_{\text{Hill}}$. For NGTS-38 b this is equivalent to a distance of $44.2 \pm 2.8 R_J$. Domingos et al. (2006) similarly find an outer limit of stability for a moon on a circular prograde orbit of $R_{\text{Hill}} \times 0.4895(1.0000 - 1.0305e)$. For NGTS-38 b we find a value of $49.2 \pm 3.2 R_J$, which we show plotted against host *Gaia* G-band magnitude in Figure 13. Both these theoretical stable regions are greater than the separation between Jupiter and Callisto, the outermost Galilean moon. This means a Galilean moon system is tentatively within the stability limits of NGTS-38 b, however given the planet's location interior to the ice line it is unclear whether such a system could form.

We also calculate the Roche limit radius for NGTS-38 b as follows:

$$d_{\text{Roche}; p} = 2.44 R_p \left(\frac{\rho_b}{\rho_{\text{sat}}} \right)^{\frac{1}{3}}, \quad (2)$$

where ρ_{sat} is the density of a satellite, which we set to $2 g \text{ cm}^{-3}$ (similar to many asteroids and planetesimals). We calculate a value of $3.50 \pm 0.28 R_J$, which is considerably larger than the limits for Jupiter ($2.13 R_J$) and Saturn ($1.39 R_J$). The Roche limit not only represents the innermost separation any potential exomoon could have without being disrupted but can also inform the extent of possible exorings. The ring systems around giant planets in the solar system tend to extend to 1-2 Roche limit radii, although proposed exoring candidates (e.g. J1407 b; Kenworthy & Mamajek 2015b) are much larger and fill the entire hill sphere of their theoretical host planets. However, if such a ring system existed around NGTS-38 b it would have almost certainly already been detectable in the existing *TESS* and NGTS photometry.

7.4.2 Detectability of moons and rings

Szabó et al. (2024) identify planets with periods > 100 days transiting stars brighter than a *Gaia* G band magnitude of 11 as high priority targets for exomoon searches. NGTS-38 b comfortably meets both of these criteria (see Figure 13). We can refine this prioritisation further by only allowing planets where the outermost prograde circular orbit radius from Domingos et al. (2006) is larger than the separation between Jupiter and the outermost Galilean moon (Callisto). This leaves only 6 high priority targets, including NGTS-38 b (see Figure 13). The other five planets in this regime are HD-114082 b (Zakhozay et al. 2022), TIC-172900988 b (Kostov et al. 2021), TOI-2010 b (Mann et al. 2023), TOI-2180 b (Dalba et al. 2022) and TOI-4465 (Essack et al. 2025). This makes NGTS-38 b one of the most exciting prospects for future exomoon surveys, although it should be noted that while the brightness of its host star will improve SNR, the large radius of the host will make detection of exomoons via the transit method more difficult. Jupiter's largest moon; Ganymede, would have a transit depth of just over 14 ppm across the sun and only ~ 4 ppm for NGTS-38.

We also considered the potential TTV signal of a Ganymede and an Earth mass moon on a circular orbit around NGTS-38 b at equal separation to that between Ganymede and Jupiter. We estimated the

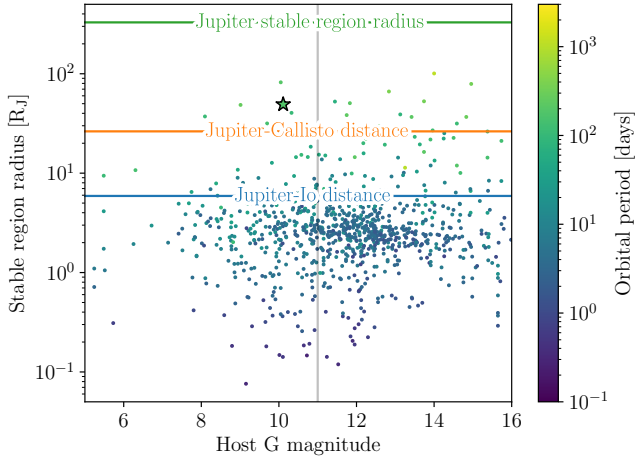


Figure 13. *Gaia* G-band magnitude plotted against stable region radius from Domingos et al. (2006) for all planets in the sample described in §6.2.1. NGTS-38 b is plotted as a black bordered star. Points are coloured according to their orbital period. A grey vertical line is plotted at $G=11$ to represent the brightness cutoff from Szabó et al. (2024). In addition, horizontal lines are plotted at $329 R_J$, $26.3 R_J$ and $5.9 R_J$ to represent the radius of the stable region for Jupiter, the distance between Jupiter and Callisto (the most widely separated Galilean moon), and the distance between Jupiter and the closest in Galilean moon; Io.

RMS amplitude of a TTV signal for both these cases using equation 3 from Kipping (2009), finding signals of 0.39 ± 0.04 s and 15.7 ± 1.5 s respectively. A signal this small would be extremely challenging to detect, making TTV exomoon detection for NGTS-38 b unlikely.

It could be possible to detect exorings around the planet by searching for abnormalities in the planet's transit shape or reflected light signals (Barnes & Fortney 2004; Aizawa et al. 2017; Akinsanmi et al. 2018; Heller 2018). We used the EXORINGS software package (Kenworthy & Mamajek 2015a,b) to model an exoring with a radius equal to d_{Roche} around NGTS-38 b, and find that this model is indistinguishable from a ringless transiting planet in *TESS*. However, with the greater photometric precision available from instruments such as *PLATO*, *JWST*, or the ELT it may be possible to detect such a system. Alternatively a spectroscopic transit observation of the RM effect, which would already be of scientific interest for constraining the orbital obliquity of the system (see Section 7.1), could be used to detect an exoring system (de Mooij et al. 2017).

8 SUMMARY AND CONCLUSIONS

TIC-65910228 b/NGTS-38 b was first detected from a single *TESS* transit in sector 33. We then initiated a campaign of spectroscopic and photometric followup that yielded an additional transit egress from NGTS and a full radial velocity solution from HARPS and CORALIE. The spectra obtained also allowed a characterisation of the host star, revealing it to have a temperature consistent with an F6V-F7V type star (6310 ± 129 K), and a low surface gravity ($\log g = 4.06 \pm 0.02$) resulting from a large radius ($1.88 \pm 0.08 R_\odot$) compared to its mass ($1.46 \pm 0.09 M_\odot$). This due to the enhanced metallicity ($[\text{Fe}/\text{H}] = 0.33 \pm 0.09$ dex) of the star. A combined fit with the photometric and spectroscopic data confirmed the planet to be a $4.78_{-0.37}^{+0.40} M_J$, $1.081 \pm 0.047 R_J$ giant planet on a 180.52791 ± 0.00038 d orbit with a moderate eccentricity of 0.308 ± 0.011 .

The planet's wide orbital separation gives it a low equilibrium temperature compared to other transiting planets, varying between 550 ± 14 K and 400 ± 10 K throughout its eccentric orbit. On account of this cooler temperature, the atmosphere is likely to contain molecular nitrogen species not found in the atmospheres of hotter giant planets. In addition, this wide separation also makes NGTS-38 b one of the most likely transiting planets to host stable exomoon and/or ring systems which could be detectable with targeted observations from high precision facilities like *PLATO*, *JWST* or the ELT.

While the planet is unsuitable for transmission spectroscopy ($\text{TSM} \sim 2.9$) with current generation instruments, there is a better chance of detecting an atmosphere through emission spectroscopy of the secondary eclipse ($\text{ESM} \sim 23$). However, perhaps the most pertinent additional observation of NGTS-38 b would be to constrain its orbital obliquity through spectroscopic transit observations. This will require extensive international collaboration to obtain longitudinal coverage from multiple facilities worldwide to observe the full ~ 15 hr transit and baseline. Although, with an estimated RM amplitude of $14 \pm 3 \text{ m s}^{-1}$ this should be possible.

NGTS-38 b's position within the LOPS2 field of the upcoming *PLATO* mission allows for the potential discovery of additional companions within the system. Either by directly detecting additional companions with transits too shallow and/or infrequent to be seen in current datasets or inferring outer companions through measuring transit timing variations of NGTS-38 b with its long baseline.

ACKNOWLEDGEMENTS

This manuscript has been prepared independently from and simultaneously with a paper on the same system from the Warm *gIaNs* with tEss (WINE) team who detected the same planet in a separate set of follow-up observations. We would like to extend our thanks to Felipe Rojas, Dr Rafael Brahm and the rest of the WINE team for agreeing to separate independent publications and for coordinating submission with us.

The author list and affiliations of this paper were created using PyTeXAUTHORS. The code is available at <https://github.com/TobyRodel/pytexauthors>.

This paper includes data collected by the *TESS* mission. Funding for the *TESS* mission is provided by the NASA Explorer Program. Resources supporting this work were provided by the NASA High-End Computing (HEC) Program through the NASA Advanced Supercomputing (NAS) Division at Ames Research Center for the production of the SPOC data products. The *TESS* team shall assure that the masses of fifty (50) planets with radii less than $4R_\oplus$ are determined.

We acknowledge the use of public *TESS* Alert data from pipelines at the *TESS* Science Office and at the *TESS* Science Processing Operations Center.

This work makes use of data from the European Space Agency (ESA) mission *Gaia* (<https://www.cosmos.esa.int/gaia>), processed by the *Gaia* Data Processing and Analysis Consortium (DPAC, <https://www.cosmos.esa.int/web/gaia/dpac/consortium>). Funding for the DPAC has been provided by national institutions, in particular the institutions participating in the *Gaia* Multilateral Agreement.

This research makes use of the Exoplanet Follow-up Observation Program website, which is operated by the California Institute of Technology, under contract with the National Aeronautics and Space Administration under the Exoplanet Exploration Program.

This paper includes data collected by the *TESS* mission that are

publicly available from the Mikulski Archive for Space Telescopes (MAST).

This work is based in part on data collected under the NGTS project at the ESO La Silla Paranal Observatory. The NGTS facility is operated by a consortium of institutes with support from the UK Science and Technology Facilities Council (STFC) under projects ST/M001962/1, ST/S002642/1 and ST/W003163/1.

This work makes use of observations from the LCOGT network. Part of the LCOGT telescope time was granted by NOIRLab through the Mid-Scale Innovations Program (MSIP). MSIP is funded by NSF.

This paper uses observations made with the Las Cumbres Observatory's education network telescopes that were upgraded through generous support from the Gordon and Betty Moore Foundation.

This research has made use of the NASA Exoplanet Archive, which is operated by the California Institute of Technology, under contract with the National Aeronautics and Space Administration under the Exoplanet Exploration Program.

TR is supported by an STFC studentship. C.A.W., E.dM., M.E.Y and J.C.C would like to acknowledge support from the UK Science and Technology Facilities Council (STFC, grant number ST/X00094X/1). JSJ gratefully acknowledges support by FONDECYT grant 1240738 and from the ANID BASAL project FB210003. ML acknowledges support of the Swiss National Science Foundation under grant number PCEFP2_194576. The contributions of ML, FB, SU and SUM have been carried out within the framework of the NCCR PlanetS supported by the Swiss National Science Foundation under grants 51NF40_182901 and 51NF40_205606. D.D., Z.E. and B.S. acknowledge support from the TESS Guest Investigator Program grant 80NSSC23K0769. D.D. also acknowledges support from TESS Guest Investigator Program grant 80NSSC22K1353. A.M. acknowledges funding from a UKRI Future Leader Fellowship, grant number MR/X033244/1 and a UK Science and Technology Facilities Council (STFC) small grant ST/Y002334/1. E.G. gratefully acknowledges support from UK Research and Innovation (UKRI) under the UK government's Horizon Europe funding guarantee for an ERC Starting Grant [grant number EP/Z000890/1]. Funding for K.B. was provided by the European Union (ERC AdG SUBSTELLAR, GA 101054354).

DATA AVAILABILITY

The *TESS* data is accessible via the MAST (Mikulski Archive for Space Telescopes) portal at <https://mast.stsci.edu/portal/Mashup/Clients/Mast/Portal.html>.

Any code used for analysis or in producing the plots in this paper can be made available upon reasonable request to the author(s).

AFFILIATIONS

¹ Astrophysics Research Centre, School of Mathematics and Physics, Queen's University Belfast, Belfast, BT7 1NN, UK

² Leiden Observatory, Leiden University, P.O. Box 9513, 2300 RA Leiden, The Netherlands

³ Observatoire de Genève, Université de Genève, 51 Ch. des Maillettes, CH-1290 Sauverny, Switzerland

⁴ Department of Physics, University of Warwick, Gibbet Hill Road, Coventry CV4 7AL, UK

⁵ Centre for Exoplanets and Habitability, University of Warwick, Gibbet Hill Road, Coventry CV4 7AL, UK

⁶ Isaac Newton Group of Telescopes, Apartado de correos 321,

E-38700 Santa Cruz de La Palma, Canary Islands; Spain

⁷ School of Physics & Astronomy, University of Birmingham, Edgbaston, Birmingham B15 2TT, UK

⁸ Center for Astrophysics | Harvard & Smithsonian, 60 Garden Street, Cambridge, MA 02138, USA

⁹ Department of Physics and Astronomy, The University of New Mexico, 210 Yale Blvd NE, Albuquerque, NM 87106, USA

¹⁰ Instituto de Astronomía, Universidad Católica del Norte, Angamos 0610, 1270709, Antofagasta, Chile

¹¹ Instituto de Astrofísica de Canarias, c/ Vía Láctea s/n, 38205 La Laguna, Tenerife, Spain

¹² Astrobiology Research Unit, Université de Liège, 19C Allée du 6 Août, 4000 Liège, Belgium

¹³ Department of Earth, Atmospheric and Planetary Science, Massachusetts Institute of Technology, 77 Massachusetts Avenue, Cambridge, MA 02139, USA

¹⁴ Astronomy Unit, Queen Mary University of London, Mile End Road, London E1 4NS, UK

¹⁵ School of Physics and Astronomy, University of Leicester, Leicester LE1 7RH, UK

¹⁶ El Sauce Observatory, Coquimbo Province, Chile

¹⁷ Rugby School, Lawrence Sheriff Street, Rugby, Warwickshire CV22 5EH, UK

¹⁸ Sapienza Università di Roma, Piazzale Aldo Moro, 5, 00185, Rome (RM), Italy

¹⁹ Campo Catino Astronomical Observatory, Regione Lazio, Guarino (FR), 03010 Italy

²⁰ INFN Sezione Roma1, Piazzale Aldo Moro, 2, 00185, Rome (RM), Italy

²¹ INAF OAC, Via della Scienza, 5, 09047, Selargius (CA), Italy

²² Instituto de Estudios Astrofísicos, Facultad de Ingeniería y Ciencias, Universidad Diego Portales, Av. Ejército Libertador 441, Santiago, Chile

²³ Centro de Excelencia en Astrofísica y Tecnologías Afines (CATA), Camino El Observatorio 1515, Las Condes, Santiago, Chile

²⁴ Columbia University, 550 W 120th Street, New York NY 10027, USA

²⁵ National Research Council Canada, Herzberg Astronomy & Astrophysics Research Centre, 5071 West Saanich Road, Victoria, BC V9E 2E7, Canada

²⁶ Subaru Telescope, National Astronomical Observatory of Japan, 650 North A'ohoku Place, Hilo, HI 96720, USA

²⁷ Departamento de Astrofísica, Universidad de La Laguna, 38206 La Laguna, Tenerife, Spain

²⁸ Hamburger Sternwarte, Gojenbergsweg 112, 21029 Hamburg, Germany

²⁹ Massachusetts Institute of Technology, Department of Physics and Kavli Institute for Astrophysics and Space Research, Cambridge, MA 02139, USA

³⁰ Centre for Space Domain Awareness, University of Warwick, Gibbet Hill Road, Coventry CV4 7AL, UK

³¹ American Association of Variable Star Observers, 49 Bay State Road, Cambridge, MA 02138, USA

³² NASA Goddard Space Flight Center, 8800 Greenbelt Road, Greenbelt, MD 20771, USA

³³ South African Astronomical Observatory, P.O Box 9, Observatory 7935, Cape Town, South Africa

REFERENCES

Acuña L., Deleuil M., Mousis O., Marcq E., Levesque M., Aguichine A., 2021, *A&A*, **647**, A53

Acuña L., Kreidberg L., Zhai M., Mollière P., 2024, *A&A*, **688**, A60

Aizawa M., Uehara S., Masuda K., Kawahara H., Suto Y., 2017, *AJ*, **153**, 193

Akeson R. L., et al., 2013, *PASP*, **125**, 989

Akinsanmi B., Oshagh M., Santos N. C., Barros S. C. C., 2018, *A&A*, **609**, A21

Albrecht S., et al., 2012a, *ApJ*, **757**, 18

Albrecht S., et al., 2012b, *ApJ*, **757**, 18

Albrecht S. H., Dawson R. I., Winn J. N., 2022, *PASP*, **134**, 082001

Aller A., Lillo-Box J., Jones D., Miranda L. F., Barceló Forteza S., 2020, *A&A*, **635**, A128

Almeida-Fernandes F., Rocha-Pinto H. J., 2018, *MNRAS*, **476**, 184

Anderson D. R., et al., 2025, NGTS-11 c: a transiting Neptune-mass planet interior to the warm Saturn NGTS-11 b ([arXiv:2510.14083](https://arxiv.org/abs/2510.14083)), <https://arxiv.org/abs/2510.14083>

Asplund M., Grevesse N., Sauval A. J., Scott P., 2009, *ARA&A*, **47**, 481

Astropy Collaboration et al., 2022, *ApJ*, **935**, 167

Barnes J. W., Fortney J. J., 2004, *The Astrophysical Journal*, **616**, 1193

Barnes J. W., O'Brien D. P., 2002, *ApJ*, **575**, 1087

Battley M. P., et al., 2024, *A&A*, **686**, A230

Bayliss D., et al., 2020, *The Messenger*, **181**, 28

Bayliss D., et al., 2022, in Holland A. D., Beletic J., eds, Society of Photo-Optical Instrumentation Engineers (SPIE) Conference Series Vol. 12191, X-Ray, Optical, and Infrared Detectors for Astronomy X. p. 121911A, doi:10.1117/12.2628966

Bensby T., Feltzing S., Lundström I., 2003, *A&A*, **410**, 527

Bensby T., Feltzing S., Oey M. S., 2014, *A&A*, **562**, A71

Benz W., et al., 2021, *Experimental Astronomy*, **51**, 109

Bieryla A., et al., 2026, arXiv e-prints, p. arXiv:2601.16357

Blanco-Cuaresma S., 2019, *MNRAS*, **486**, 2075

Blanco-Cuaresma S., Soubiran C., Heiter U., Jofré P., 2014, *A&A*, **569**, A111

Blunt S., Wang J., Murray-Clay R., Macintosh B., Rubenzahl R. A., Fulton B. J., 2026, arXiv e-prints, p. arXiv:2601.18877

Bobylev V. V., Bajkova A. T., 2014, *MNRAS*, **441**, 142

Bodenheimer P., Hubickyj O., Lissauer J. J., 2000, *Icarus*, **143**, 2

Börner A., et al., 2024, *Experimental Astronomy*, **58**, 1

Brahm R., et al., 2023, *AJ*, **165**, 227

Brown T. M., et al., 2013, *PASP*, **125**, 1031

Bryant E. M., et al., 2020, *MNRAS*, **494**, 5872

Caldwell D. A., et al., 2020, *Research Notes of the American Astronomical Society*, **4**, 201

Chabrier G., Debras F., 2021, *ApJ*, **917**, 4

Charbonneau D., Brown T. M., Noyes R. W., Gilliland R. L., 2002, *ApJ*, **568**, 377

Chen D.-C., et al., 2021, *ApJ*, **909**, 115

Choi J., Dotter A., Conroy C., Cantiello M., Paxton B., Johnson B. D., 2016, *ApJ*, **823**, 102

Christiansen J. L., et al., 2025, *The Planetary Science Journal*, **6**, 186

Claytor Z. R., van Saders J. L., Santos Á. R. G., García R. A., Mathur S., Tayar J., Pinsonneault M. H., Shetrone M., 2020, *ApJ*, **888**, 43

Coşkunoğlu B., et al., 2011, *MNRAS*, **412**, 1237

Collins K., 2019, in American Astronomical Society Meeting Abstracts #233. p. 140.05

Collins K. A., Kielkopf J. F., Stassun K. G., Hessman F. V., 2017, *The Astronomical Journal*, **153**, 77

Cooke B. F., Pollacco D., West R., McCormac J., Wheatley P. J., 2018, *A&A*, **619**, A175

Cooke B. F., Pollacco D., Bayliss D., 2019, *A&A*, **631**, A83

Cooke B. F., et al., 2021, *MNRAS*, **500**, 5088

Dalba P. A., et al., 2021, *AJ*, **162**, 154

Dalba P. A., et al., 2022, *AJ*, **163**, 61

Dawson R. I., Johnson J. A., 2018, *ARA&A*, **56**, 175

Demarque P., Guenther D. B., Li L. H., Mazumdar A., Straka C. W., 2008, *Ap&SS*, **316**, 31

Dewberry J. W., 2024, *ApJ*, **966**, 180

Domingos R. C., Winter O. C., Yokoyama T., 2006, *MNRAS*, **373**, 1227

Dotter A., 2016, *ApJS*, **222**, 8

Dotter A., Chaboyer B., Jevremović D., Kostov V., Baron E., Ferguson J. W., 2008, *ApJS*, **178**, 89

Doyle L., Armstrong D. J., Bayliss D., Rodel T., Kunovac V., 2024, *MNRAS*, **529**, 1802

Eberhardt J., et al., 2023, *AJ*, **166**, 271

Eschen Y. N. E., Bayliss D., Wilson T. G., Kunimoto M., Pelisoli I., Rodel T., 2024, *MNRAS*, **535**, 1778

Eschen Y. N. E., et al., 2025, *MNRAS*, **544**, 2614

Espinosa-Retamal J. I., et al., 2025, *AJ*, **170**, 70

Essack Z., et al., 2025, *AJ*, **170**, 41

Feinstein A. D., et al., 2019, *PASP*, **131**, 094502

Fortney J. J., Visscher C., Marley M. S., Hood C. E., Line M. R., Thorngren D. P., Freedman R. S., Lupu R., 2020, *AJ*, **160**, 288

Francis C., Anderson E., 2014, *Celestial Mechanics and Dynamical Astronomy*, **118**, 399

Freckleton A. V., et al., 2024, *MNRAS*, **531**, 4085

Freckleton A. V., et al., 2025, *MNRAS*, **540**, 1786

Gaia Collaboration et al., 2021, *A&A*, **649**, A1

Gill S., et al., 2020a, *MNRAS*, **491**, 1548

Gill S., et al., 2020b, *MNRAS*, **495**, 2713

Gill S., et al., 2020c, *ApJ*, **898**, L11

Gill S., et al., 2022, *MNRAS*, **513**, 1785

Gill S., et al., 2024, *MNRAS*, **532**, 1444

Goldreich P., Tremaine S., 1980, *ApJ*, **241**, 425

Gong Y.-X., Zhou J.-L., Xie J.-W., Wu X.-M., 2013, *ApJ*, **769**, L14

Grieves N., et al., 2022, *A&A*, **668**, A29

Grouffal S., et al., 2022, *A&A*, **668**, A172

Grouffal S., et al., 2025, *A&A*, **701**, A173

Guillot T., Burrows A., Hubbard W. B., Lunine J. I., Saumon D., 1996, *ApJ*, **459**, L35

Günther M. N., Daylan T., 2019, Allesfitter: Flexible Star and Exoplanet Inference From Photometry and Radial Velocity, *Astrophysics Source Code Library* (ascl:1903.003)

Günther M. N., Daylan T., 2021, *ApJS*, **254**, 13

Haldemann J., Alibert Y., Mordasini C., Benz W., 2020, *A&A*, **643**, A105

Hawthorn F., et al., 2024, *MNRAS*, **528**, 1841

Heller R., 2018, in Deeg H. J., Belmonte J. A., eds, *Handbook of Exoplanets*. Springer Cham, p. 35, doi:10.1007/978-3-319-55333-7_35

Henden A., Munari U., 2014, *Contributions of the Astronomical Observatory Skalnate Pleso*, **43**, 518

Henderson B. A., et al., 2024, *MNRAS*, **533**, 2823

Hertzsprung E., 1913, *Astronomische Nachrichten*, **196**, 201

Hippke M., Heller R., 2019, *A&A*, **623**, A39

Hippke M., David T. J., Mulders G. D., Heller R., 2019, *AJ*, **158**, 143

Hobson M. J., et al., 2021, *AJ*, **161**, 235

Høg E., et al., 2000, *A&A*, **355**, L27

Huang C., Wu Y., Triaud A. H. M. J., 2016, *ApJ*, **825**, 98

Jackson B., Greenberg R., Barnes R., 2008, *The Astrophysical Journal*, **678**, 1396

Jenkins J. S., et al., 2006, *MNRAS*, **372**, 163

Jenkins J. S., Jones H. R. A., Pavlenko Y., Pinfield D. J., Barnes J. R., Lyubchik Y., 2008, *A&A*, **485**, 571

Jenkins J. S., et al., 2011, *A&A*, **531**, A8

Jenkins J. M., et al., 2016, in Chiozzi G., Guzman J. C., eds, Society of Photo-Optical Instrumentation Engineers (SPIE) Conference Series Vol. 9913, *Software and Cyberinfrastructure for Astronomy IV*. p. 99133E, doi:10.1117/12.2233418

Johnson D. R. H., Soderblom D. R., 1987, *AJ*, **93**, 864

Kaufer A., Stahl O., Tubbesing S., Nørregaard P., Avila G., Francois P., Pasquini L., Pizzella A., 1999, *The Messenger*, **95**, 8

Keller S. C., et al., 2007, *Publ. Astron. Soc. Australia*, **24**, 1

Kempton E. M.-R., et al., 2018, *PASP*, **130**, 114401

Kendall A., et al., 2025, arXiv e-prints, p. arXiv:2512.07716

Kenworthy M. A., Mamajek E. E., 2015a, *Exorings: Exoring modelling software*, *Astrophysics Source Code Library*, record ascl:1501.012

Kenworthy M. A., Mamajek E. E., 2015b, *ApJ*, **800**, 126

Kipping D. M., 2009, *MNRAS*, **392**, 181

Kipping D. M., 2013, *MNRAS*, **435**, 2152

Knudstrup E., et al., 2024, *A&A*, **690**, A379

Kochanek C. S., et al., 2017, *PASP*, **129**, 104502

Kostov V. B., et al., 2021, *AJ*, **162**, 234

Koval' V. V., Marsakov V. A., Borkova T. V., 2009, *Astronomy Reports*, **53**, 1117

Kozai Y., 1962, *AJ*, **67**, 591

Kraft R. P., 1967, *ApJ*, **150**, 551

Lendl M., et al., 2020, *MNRAS*, **492**, 1761

Lidov M. L., 1962, *Planet. Space Sci.*, **9**, 719

Lindegren L., 2020, *A&A*, **633**, A1

Lindegren L., et al., 2021, *A&A*, **649**, A2

Lomb N. R., 1976, *Ap&SS*, **39**, 447

Mann C. R., et al., 2023, *AJ*, **166**, 239

Maxted P. F. L., 2016, *A&A*, **591**, A111

Mayor M., Queloz D., 1995, *Nature*, **378**, 355

Mayor M., et al., 2003, *The Messenger*, **114**, 20

McCullry C., Volgenau N. H., Harbeck D.-R., Lister T. A., Saunders E. S., Turner M. L., Siiverd R. J., Bowman M., 2018, in Guzman J. C., Ibsen J., eds, Society of Photo-Optical Instrumentation Engineers (SPIE) Conference Series Vol. 10707, Software and Cyberinfrastructure for Astronomy V. p. 107070K ([arXiv:1811.04163](https://arxiv.org/abs/1811.04163)), doi:10.1111/12.2314340

McLaughlin D. B., 1924, *ApJ*, **60**, 22

Montalvo M., et al., 2021, *A&A*, **653**, A98

Mordasini C., Alibert Y., Klahr H., Henning T., 2012, *A&A*, **547**, A111

Mortier A., Sousa S. G., Adibekyan V. Z., Brandão I. M., Santos N. C., 2014, *A&A*, **572**, A95

Morton T. D., 2015, isochrones: Stellar model grid package, Astrophysics Source Code Library, record ascl:1503.010 (ascl:1503.010)

Naoz S., 2016, *ARA&A*, **54**, 441

Narang M., Manoj P., Furlan E., Mordasini C., Henning T., Mathew B., Banyal R. K., Sivarani T., 2018, *AJ*, **156**, 221

Nascimbeni V., et al., 2025, *A&A*, **694**, A313

O'Brien S. M., et al., 2022, *MNRAS*, **509**, 6111

Öberg K. I., Murray-Clay R., Bergin E. A., 2011, *ApJ*, **743**, L16

Onken C. A., Wolf C., Bessell M. S., Chang S.-W., Luval L. C., Tonry J. L., White M. C., Da Costa G. S., 2024, *Publ. Astron. Soc. Australia*, **41**, e061

Osborn H. P., et al., 2023, *MNRAS*, **523**, 3069

Parviainen H., Aigrain S., 2015, *MNRAS*, **453**, 3821

Paxton B., Bildsten L., Dotter A., Hervig F., Lesaffre P., Timmes F., 2010, MESA: Modules for Experiments in Stellar Astrophysics, Astrophysics Source Code Library, record ascl:1010.083 (ascl:1010.083)

Pecaut M. J., Mamajek E. E., 2013, *ApJS*, **208**, 9

Pepe F., et al., 2000, in Iye M., Moorwood A. F., eds, Society of Photo-Optical Instrumentation Engineers (SPIE) Conference Series Vol. 4008, Optical and IR Telescope Instrumentation and Detectors. pp 582–592, doi:10.1111/12.395516

Pepe F., et al., 2021, *A&A*, **645**, A96

Pierrehumbert R. T., Hammond M., 2019, *Annual Review of Fluid Mechanics*, **51**, 275

Pollacco D. L., et al., 2006, *PASP*, **118**, 1407

Queloz D., et al., 2001, *The Messenger*, **105**, 1

Rasio F. A., Ford E. B., 1996, *Science*, **274**, 954

Rauer H., et al., 2025, *Experimental Astronomy*, **59**, 26

Reddy B. E., Lambert D. L., Allende Prieto C., 2006, *MNRAS*, **367**, 1329

Rice M., et al., 2022, *AJ*, **164**, 104

Ricker G. R., et al., 2015, *Journal of Astronomical Telescopes, Instruments, and Systems*, **1**, 014003

Rodel T., Bayliss D., Gill S., Hawthorn F., 2024, *MNRAS*, **529**, 715

Rodel T., et al., 2025, *MNRAS*, **537**, 35

Rosario-Franco M., Quarles B., Musielak Z. E., Cuntz M., 2020, *AJ*, **159**, 260

Rossiter R. A., 1924, *ApJ*, **60**, 15

Russell H. N., 1913, *The Observatory*, **36**, 324

Santos N. C., et al., 2017, *A&A*, **603**, A30

Sanz-Forcada J., Micela G., Ribas I., Pollock A. M. T., Eiroa C., Velasco A., Solano E., García-Álvarez D., 2011, *A&A*, **532**, A6

Scargle J. D., 1982, *ApJ*, **263**, 835

Schlaufman K. C., 2018, *ApJ*, **853**, 37

Schlecker M., et al., 2020, *AJ*, **160**, 275

Schönrich R., Binney J., Dehnen W., 2010, *MNRAS*, **403**, 1829

Showman A. P., Tan X., Parmentier V., 2020, *Space Sci. Rev.*, **216**, 139

Skilling J., 2004, in Fischer R., Preuss R., Toussaint U. V., eds, American Institute of Physics Conference Series Vol. 735, Bayesian Inference and Maximum Entropy Methods in Science and Engineering: 24th International Workshop on Bayesian Inference and Maximum Entropy Methods in Science and Engineering. AIP, pp 395–405, doi:10.1063/1.1835238

Skilling J., 2006, *Bayesian Anal.*, **1**, 833

Skrutskie M. F., et al., 2006, *AJ*, **131**, 1163

Speagle J. S., 2020, *MNRAS*, **493**, 3132

Stassun K. G., et al., 2019, *AJ*, **158**, 138

Szabó G. M., Schneider J., Denes Z., Kálmán S., 2024, *Universe*, **10**, 110

Tayar J., Claytor Z. R., Huber D., van Saders J., 2022, *ApJ*, **927**, 31

Tian H.-J., et al., 2015, *ApJ*, **809**, 145

Torres G., Fischer D. A., Sozzetti A., Buchhave L. A., Winn J. N., Holman M. J., Carter J. A., 2012, *ApJ*, **757**, 161

Triaud A. H. M. J., 2018, in Deeg H. J., Belmonte J. A., eds, , *Handbook of Exoplanets*. Springer Cham, p. 2, doi:10.1007/978-3-319-55333-7_2

Tuson A., et al., 2023, *MNRAS*, **523**, 3090

Ulmer-Moll S., et al., 2022, *A&A*, **666**, A46

Ulmer-Moll S., et al., 2023, *A&A*, **674**, A43

Ulmer-Moll S., et al., 2025, [arXiv e-prints](https://arxiv.org/abs/2509.15424), p. arXiv:2509.15424

Villanueva Jr. S., Dragomir D., Gaudi B. S., 2019, *AJ*, **157**, 84

Wang X.-Y., et al., 2024, *ApJ*, **973**, L21

Watson C. A., Littlefair S. P., Collier Cameron A., Dhillon V. S., Simpson E. K., 2010, *MNRAS*, **408**, 1606

Weiss A., Schlattl H., 2008, *Ap&SS*, **316**, 99

Wheatley P. J., et al., 2018, *MNRAS*, **475**, 4476

Winn J. N., 2014, in Seager S., ed., , *Exoplanets*. University of Arizona Press, pp 55–77, doi:10.48550/arXiv.1001.2010

Winn J. N., Fabrycky D. C., 2015, *ARA&A*, **53**, 409

Winn J. N., Fabrycky D., Albrecht S., Johnson J. A., 2010, *ApJ*, **718**, L145

Wright E. L., et al., 2010, *AJ*, **140**, 1868

Zakhzhay O. V., et al., 2022, *A&A*, **667**, L14

Zechmeister M., Kürster M., 2009, *A&A*, **496**, 577

de Mooij E. J. W., Watson C. A., Kenworthy M. A., 2017, *MNRAS*, **472**, 2713

Table A1. NGTS data.

ActionID	Camera	Time BJD	Relative Flux	Normalised Flux	Airmass	Sky Background e ⁻ counts	FWHM Pixels
<i>Run 1</i>							
354981	809	2460182.87854167	0.02155 ± 0.00026	1.002 ± 0.012	1.98486	30572.598	2.0288
354981	809	2460182.87877315	0.02177 ± 0.00026	1.012 ± 0.012	1.9807	30488.725	1.9034
354981	809	2460182.87892361	0.02162 ± 0.00026	1.005 ± 0.012	1.97804	30561.318	1.9016
354981	809	2460182.87907407	0.02140 ± 0.00026	0.995 ± 0.012	1.97533	30451.943	1.9763
354981	809	2460182.87922454	0.02146 ± 0.00026	0.998 ± 0.012	1.97268	30389.973	1.9915
...
<i>Run 2</i>							
371970	809	2460417.47934028	0.01771 ± 0.00009	0.993 ± 0.005	1.04657	31509.871	1.7379
371970	809	2460417.47966435	0.01789 ± 0.00009	1.002 ± 0.005	1.04714	30847.371	1.7083
371970	809	2460417.47993056	0.01784 ± 0.00009	1.000 ± 0.005	1.0476	30342.18	1.7198
371970	809	2460417.48008102	0.01776 ± 0.00009	0.995 ± 0.005	1.04786	30145.863	1.7168
371970	809	2460417.48023148	0.01781 ± 0.00009	0.998 ± 0.005	1.04813	29873.92	1.7392
...
<i>Run 3</i>							
380563	809	2460541.9097338	0.02013 ± 0.00026	1.018 ± 0.013	1.75903	67949.33	2.0486
380563	809	2460541.90997685	0.01997 ± 0.00026	1.010 ± 0.013	1.75561	67824.34	2.0401
380563	809	2460541.91012731	0.01986 ± 0.00025	1.004 ± 0.013	1.75361	67808.19	2.0626
380563	809	2460541.91027778	0.01980 ± 0.00025	1.002 ± 0.013	1.7516	68065.3	1.9862
380563	809	2460541.91042824	0.01966 ± 0.00025	0.994 ± 0.013	1.7496	67986.94	2.0328
...
<i>Run 4</i>							
389750	809	2460637.63924769	0.01995 ± 0.00023	1.013 ± 0.011	1.9713	20280.932	1.9383
389750	809	2460637.63939815	0.01961 ± 0.00022	0.995 ± 0.011	1.96865	20225.166	1.8716
389750	809	2460637.63954861	0.01984 ± 0.00022	1.007 ± 0.011	1.96599	20302.121	1.9032
389750	809	2460637.63969907	0.01976 ± 0.00022	1.003 ± 0.011	1.96334	20340.297	1.9533
389750	809	2460637.63984954	0.01978 ± 0.00022	1.004 ± 0.011	1.96071	20321.646	1.9033
...
<i>Run 5</i>							
422211	806	2461012.61271991	0.01583 ± 0.00021	1.017 ± 0.013	1.97804	56994.95	1.8726
422211	806	2461012.61297454	0.01530 ± 0.00020	0.983 ± 0.013	1.9736	56874.996	1.8558
422211	806	2461012.61311343	0.01542 ± 0.00020	0.991 ± 0.013	1.97096	56803.188	1.8159
422211	806	2461012.61326389	0.01541 ± 0.00020	0.990 ± 0.013	1.96832	56776.184	1.853
422211	806	2461012.61341435	0.01558 ± 0.00021	1.001 ± 0.013	1.96568	56766.62	1.8438
...

APPENDIX A: NGTS PHOTOMETRIC DATA

In Table A1 we show the NGTS data for NGTS-38 separated into the runs shown in Table 1. The table is truncated in print to only the first five rows for each run, however, full machine readable versions will be made available online.

ActionID is an identification number given to each night of observations from each telescope. Camera is the ID of the telescope making the observations, in runs 1-3 this is only 809 while run 4 contains 809 and 810. Timestamps are listed in BJD. Relative Flux is the ‘raw’ flux output of the BSPROC pipeline and is the target counts divided by the total master comparison counts. Normalised Flux is this relative flux median normalised for each run. The Sky background is given as the total number of electron counts for that exposure. The FWHM is measured (in pixels) by creating a super-sampled Point Spread Function (PSF) across the central third of the image.

APPENDIX B: RADIAL VELOCITY DATA

Here we present the radial velocity timeseries data from both CORALIE (Table B1) and HARPS (Table B2). These tables will be available online in a machine readable format.

For both datasets Time is the Time in TBJD (i.e. BJD-2457000) rounded to 3 decimal places and RV is the radial velocity in km s⁻¹. For HARPS we list the exposure time T_{exp} in minutes for each spectrum whilst we omit this for CORALIE as every spectrum was taken with an exposure time of 20 minutes. For CORALIE SNR₆₂ is the signal to noise ratio of spectral order 62 and for HARPS SNR₆₄ is the signal to noise ratio of spectral order 64. For both datasets, ‘Airmass’ is the airmass at the midpoint of the exposure for each spectrum. FWHM and BIS are the Full Width Half Maximum and Bisector Inverse Slopes of the Cross Correlation Function used to determine the RVs of each spectrum in

Table B1. CORALIE data.

Time (TBJD)	RV km s^{-1}	SNR ₆₂	Airmass	FWHM km s^{-1}	BIS m s^{-1}	Contrast	H α index	Na index	Ca index	Berv m s^{-1}
CORALIE ₁₄										
3050.559	20.15 ± 0.03	23.3	1.29	12.87 ± 0.02	25 ± 39	24.71	0.180 ± 0.004	0.372 ± 0.005	0.026 ± 0.008	-18.87
3289.700	20.04 ± 0.02	31.8	1.11	12.84 ± 0.02	2 ± 22	24.77	0.184 ± 0.003	0.372 ± 0.003	0.130 ± 0.004	11.72
3310.870	19.99 ± 0.01	36.1	1.41	12.88 ± 0.02	-20 ± 20	24.47	0.178 ± 0.003	0.358 ± 0.003	0.142 ± 0.004	5.05
3367.677	19.91 ± 0.02	34.5	1.20	12.91 ± 0.02	64 ± 23	24.38	0.185 ± 0.003	0.363 ± 0.003	0.136 ± 0.005	-12.48
3381.711	19.99 ± 0.02	35.3	1.74	12.95 ± 0.02	79 ± 23	24.33	0.183 ± 0.003	0.360 ± 0.003	0.131 ± 0.006	-15.63
3394.672	20.11 ± 0.01	37.9	1.76	12.86 ± 0.02	-10 ± 21	24.39	0.178 ± 0.003	0.354 ± 0.003	0.135 ± 0.005	-17.60
3397.533	20.12 ± 0.02	31.6	1.03	12.83 ± 0.02	23 ± 26	24.47	0.170 ± 0.003	0.350 ± 0.003	0.199 ± 0.006	-17.71
3401.571	20.17 ± 0.01	40.4	1.15	12.95 ± 0.02	21 ± 20	24.36	0.179 ± 0.003	0.354 ± 0.003	0.125 ± 0.004	-18.19
3404.563	20.16 ± 0.01	39.2	1.16	12.87 ± 0.02	-27 ± 20	24.44	0.187 ± 0.003	0.352 ± 0.003	0.107 ± 0.004	-18.42
3409.578	20.19 ± 0.03	23.5	1.28	12.90 ± 0.02	-37 ± 40	24.51	0.180 ± 0.004	0.349 ± 0.004	0.127 ± 0.009	-18.74
3424.509	20.18 ± 0.02	34.3	1.16	12.90 ± 0.02	-10 ± 25	24.26	0.188 ± 0.003	0.359 ± 0.003	0.132 ± 0.005	-18.66
3428.525	20.15 ± 0.02	30.5	1.29	12.84 ± 0.02	43 ± 29	24.55	0.176 ± 0.003	0.344 ± 0.004	0.135 ± 0.006	-18.50
3435.482	20.15 ± 0.02	35.2	1.18	12.86 ± 0.02	29 ± 23	24.52	0.178 ± 0.003	0.365 ± 0.003	0.144 ± 0.005	-17.91
CORALIE ₂₄										
3605.815	20.15 ± 0.02	24.9	1.17	12.92 ± 0.02	65 ± 32	24.54	0.192 ± 0.004	0.382 ± 0.004	0.128 ± 0.006	18.93
3614.759	20.14 ± 0.03	19.6	1.32	12.86 ± 0.02	-7 ± 43	24.68	0.185 ± 0.005	0.376 ± 0.005	0.162 ± 0.010	18.64
3621.745	20.10 ± 0.02	31.1	1.29	12.78 ± 0.02	-11 ± 24	24.57	0.191 ± 0.003	0.355 ± 0.003	0.162 ± 0.005	18.03
3630.687	20.10 ± 0.02	25.9	1.55	12.89 ± 0.02	65 ± 29	24.72	0.182 ± 0.004	0.363 ± 0.004	0.103 ± 0.007	16.93
3637.713	20.10 ± 0.02	31.3	1.23	12.87 ± 0.02	-1 ± 23	24.55	0.190 ± 0.003	0.370 ± 0.003	0.150 ± 0.005	15.68
3659.727	19.98 ± 0.01	33.7	1.02	12.84 ± 0.02	-28 ± 21	24.60	0.184 ± 0.003	0.367 ± 0.003	0.137 ± 0.004	10.35
3666.641	20.01 ± 0.02	27.9	1.20	12.81 ± 0.02	-18 ± 26	24.72	0.190 ± 0.004	0.355 ± 0.004	0.135 ± 0.005	8.50
3677.697	19.99 ± 0.02	27.8	1.00	12.84 ± 0.02	0 ± 27	24.66	0.183 ± 0.004	0.348 ± 0.004	0.150 ± 0.006	4.88
3684.604	19.95 ± 0.02	26.3	1.16	12.81 ± 0.02	0 ± 28	24.72	0.183 ± 0.004	0.346 ± 0.004	0.140 ± 0.006	2.78
3694.556	19.97 ± 0.02	29.5	1.25	12.89 ± 0.02	28 ± 25	24.62	0.174 ± 0.003	0.352 ± 0.003	0.138 ± 0.005	-0.47
3703.620	19.90 ± 0.01	34.2	1.01	12.82 ± 0.02	42 ± 21	24.62	0.181 ± 0.003	0.349 ± 0.003	0.123 ± 0.004	-3.63
3710.719	19.91 ± 0.02	29.3	1.13	12.83 ± 0.02	21 ± 26	24.60	0.178 ± 0.003	0.352 ± 0.004	0.171 ± 0.006	-6.16
3715.699	19.92 ± 0.04	15.3	1.11	12.83 ± 0.02	65 ± 63	24.44	0.183 ± 0.006	0.349 ± 0.006	0.131 ± 0.015	-7.67
3722.634	19.92 ± 0.02	28.3	1.02	12.85 ± 0.02	-54 ± 26	24.57	0.179 ± 0.004	0.350 ± 0.004	0.121 ± 0.005	-9.60
3727.647	19.91 ± 0.02	31.0	1.06	12.89 ± 0.02	-10 ± 22	24.60	0.175 ± 0.003	0.348 ± 0.003	0.148 ± 0.004	-11.03
3734.658	19.93 ± 0.02	27.3	1.15	12.92 ± 0.02	58 ± 27	24.59	0.184 ± 0.004	0.352 ± 0.004	0.132 ± 0.006	-12.88
3747.587	20.02 ± 0.02	30.4	1.05	12.82 ± 0.02	61 ± 24	24.57	0.181 ± 0.003	0.359 ± 0.003	0.150 ± 0.005	-15.54
3754.633	20.08 ± 0.01	34.9	1.28	12.92 ± 0.02	51 ± 20	24.56	0.184 ± 0.003	0.352 ± 0.003	0.142 ± 0.004	-16.82
3760.643	20.17 ± 0.02	23.3	1.47	12.87 ± 0.02	22 ± 33	24.62	0.178 ± 0.004	0.362 ± 0.004	0.127 ± 0.008	-17.66
3765.528	20.17 ± 0.02	22.5	1.04	12.93 ± 0.02	43 ± 35	24.58	0.184 ± 0.004	0.360 ± 0.005	0.085 ± 0.007	-17.99
3773.532	20.18 ± 0.02	33.4	1.09	12.88 ± 0.02	13 ± 22	24.57	0.186 ± 0.003	0.371 ± 0.003	0.133 ± 0.005	-18.58
3777.505	20.16 ± 0.02	28.4	1.05	12.86 ± 0.02	29 ± 27	24.58	0.193 ± 0.004	0.362 ± 0.004	0.151 ± 0.006	-18.69
3782.499	20.18 ± 0.02	32.9	1.07	12.89 ± 0.02	6 ± 23	24.47	0.182 ± 0.003	0.359 ± 0.003	0.115 ± 0.005	-18.76
3784.553	20.16 ± 0.03	22.8	1.31	12.87 ± 0.02	-13 ± 37	24.53	0.183 ± 0.004	0.372 ± 0.005	0.085 ± 0.008	-18.85
3789.497	20.16 ± 0.02	26.6	1.12	12.91 ± 0.02	-16 ± 30	24.56	0.189 ± 0.004	0.359 ± 0.004	0.154 ± 0.007	-18.66
3795.509	20.13 ± 0.02	29.1	1.23	12.90 ± 0.02	-17 ± 27	24.62	0.182 ± 0.004	0.360 ± 0.004	0.127 ± 0.006	-18.37
3801.496	20.14 ± 0.02	28.5	1.25	12.89 ± 0.02	-2 ± 28	24.48	0.181 ± 0.004	0.367 ± 0.004	0.122 ± 0.006	-17.85
3808.494	20.13 ± 0.02	28.6	1.35	12.90 ± 0.02	7 ± 29	24.18	0.189 ± 0.004	0.362 ± 0.004	0.181 ± 0.007	-17.03
3818.465	20.09 ± 0.02	33.1	1.35	12.87 ± 0.02	10 ± 24	24.40	0.182 ± 0.003	0.353 ± 0.003	0.153 ± 0.006	-15.46
3826.444	20.05 ± 0.02	30.2	1.34	12.81 ± 0.02	68 ± 28	24.23	0.184 ± 0.003	0.360 ± 0.004	0.148 ± 0.007	-13.88
3834.458	20.03 ± 0.02	27.9	1.66	12.90 ± 0.02	25 ± 32	24.24	0.186 ± 0.004	0.363 ± 0.004	0.094 ± 0.009	-12.09
3949.836	20.13 ± 0.02	23.2	1.34	12.83 ± 0.02	20 ± 33	24.61	0.183 ± 0.004	0.369 ± 0.004	0.215 ± 0.008	18.06
3957.846	20.18 ± 0.02	29.0	1.17	12.86 ± 0.02	-20 ± 25	24.60	0.185 ± 0.004	0.375 ± 0.004	0.126 ± 0.005	18.64
3964.873	20.16 ± 0.02	29.2	1.05	12.82 ± 0.02	-17 ± 25	24.56	0.191 ± 0.004	0.368 ± 0.004	0.131 ± 0.005	18.84

km s^{-1} and m s^{-1} respectively. For Both datasets we also include the Contrast as well as the Hydrogen alpha, Sodium and Calcium indexes as dimensionless quantities. We list the Barycentric Radial Velocity correction (Berv) in m s^{-1} for both datasets. For HARPS we also include the $\log R'_{\text{HK}}$ value calculated for each spectra.

Table B2. HARPS data.

Time (TBJD)	RV km s^{-1}	T_{exp} (mins)	SNR_{64}	Airmass	FWHM km s^{-1}	BIS m s^{-1}	Contrast	$\text{H}\alpha$ index	Na index	Ca index	Berv m s^{-1}	$\log R'_{\text{HK}}$
3299.723	19.916 ± 0.003	25	75.5	1.02	12.56 ± 0.01	2 ± 7	37.55	0.1926 ± 0.0002	0.3924 ± 0.0002	0.1084 ± 0.0004	8.82	-5.012 ± 0.003
3325.788	19.838 ± 0.004	25	63.6	1.19	12.58 ± 0.01	-13 ± 8	37.53	0.1951 ± 0.0003	0.3912 ± 0.0002	0.1059 ± 0.0006	0.22	-5.032 ± 0.005
3328.702	19.848 ± 0.004	25	56.8	1.01	12.55 ± 0.01	3 ± 9	37.51	0.1976 ± 0.0003	0.3893 ± 0.0002	0.1077 ± 0.0006	-0.59	-5.017 ± 0.005
3331.723	19.828 ± 0.005	25	51.4	1.05	12.54 ± 0.01	-8 ± 10	37.49	0.1981 ± 0.0004	0.3896 ± 0.0003	0.1072 ± 0.0007	-1.65	-5.022 ± 0.006
3342.747	19.817 ± 0.004	25	75.9	1.21	12.59 ± 0.01	-15 ± 7	37.54	0.1911 ± 0.0002	0.3890 ± 0.0002	0.1067 ± 0.0005	-5.33	-5.026 ± 0.004
3346.790	19.809 ± 0.005	25	58.9	1.59	12.54 ± 0.01	-6 ± 10	37.56	0.1937 ± 0.0003	0.3894 ± 0.0002	0.0993 ± 0.0010	-6.68	-5.090 ± 0.009
3350.712	19.804 ± 0.003	25	78.4	1.16	12.58 ± 0.01	5 ± 7	37.48	0.1932 ± 0.0002	0.3875 ± 0.0002	0.1056 ± 0.0005	-7.78	-5.035 ± 0.004
3375.668	19.835 ± 0.004	20	65.1	1.27	12.56 ± 0.01	3 ± 8	37.55	0.1938 ± 0.0002	0.3902 ± 0.0002	0.1067 ± 0.0006	-14.34	-5.026 ± 0.005
3380.527	19.863 ± 0.004	20	53.2	1.00	12.57 ± 0.01	-1 ± 9	37.57	0.1966 ± 0.0003	0.3917 ± 0.0003	0.1101 ± 0.0005	-15.07	-4.999 ± 0.004
3598.796	20.071 ± 0.005	20	46.1	1.36	12.54 ± 0.01	13 ± 11	37.59	0.2033 ± 0.0004	0.3990 ± 0.0003	0.0924 ± 0.0008	18.95	-5.161 ± 0.009
3601.803	20.057 ± 0.005	20	44.9	1.26	12.54 ± 0.01	-13 ± 11	37.62	0.2019 ± 0.0004	0.4011 ± 0.0003	0.0906 ± 0.0008	18.98	-5.182 ± 0.009
3614.774	20.044 ± 0.006	20	42.7	1.24	12.58 ± 0.01	-5 ± 12	37.58	0.2035 ± 0.0004	0.3991 ± 0.0004	0.0964 ± 0.0010	18.61	-5.119 ± 0.010
3660.672	19.918 ± 0.004	20	55.0	1.15	12.58 ± 0.01	-1 ± 9	37.56	0.1986 ± 0.0003	0.3940 ± 0.0003	0.0937 ± 0.0006	10.19	-5.147 ± 0.007
3702.720	19.830 ± 0.005	20	53.0	1.07	12.58 ± 0.01	-0 ± 9	37.58	0.1951 ± 0.0003	0.3994 ± 0.0002	0.1025 ± 0.0008	-3.55	-5.061 ± 0.007
3731.658	19.826 ± 0.005	20	52.8	1.13	12.57 ± 0.01	11 ± 9	37.58	0.1959 ± 0.0003	0.4010 ± 0.0003	0.0945 ± 0.0007	-12.12	-5.138 ± 0.008
3737.647	19.847 ± 0.005	20	49.7	1.14	12.56 ± 0.01	12 ± 10	37.56	0.1989 ± 0.0003	0.3977 ± 0.0003	0.0945 ± 0.0009	-13.57	-5.139 ± 0.009
3747.656	19.925 ± 0.004	20	59.0	1.31	12.58 ± 0.01	-12 ± 9	37.45	0.1930 ± 0.0003	0.4009 ± 0.0002	0.0987 ± 0.0008	-15.67	-5.097 ± 0.007
3753.588	19.983 ± 0.005	20	52.2	1.10	12.57 ± 0.01	-14 ± 9	37.46	0.1983 ± 0.0003	0.4067 ± 0.0002	0.0833 ± 0.0007	-16.57	-5.277 ± 0.010
3765.630	20.063 ± 0.005	20	49.9	1.49	12.53 ± 0.01	-8 ± 11	37.51	0.1997 ± 0.0004	0.4040 ± 0.0003	0.0872 ± 0.0010	-18.17	-5.223 ± 0.013
3784.578	20.063 ± 0.008	20	35.3	1.49	12.55 ± 0.02	11 ± 16	37.67	0.2046 ± 0.0006	0.4073 ± 0.0004	0.0643 ± 0.0018	-18.89	-5.716 ± 0.071
3800.528	20.029 ± 0.004	20	63.2	1.45	12.58 ± 0.01	2 ± 8	37.46	0.1925 ± 0.0002	0.4099 ± 0.0002	0.0921 ± 0.0007	-17.99	-5.165 ± 0.008
3801.463	20.034 ± 0.004	20	57.0	1.13	12.55 ± 0.01	-11 ± 8	37.53	0.1934 ± 0.0003	0.4078 ± 0.0002	0.0900 ± 0.0006	-17.79	-5.189 ± 0.007
4045.820	19.862 ± 0.005	20	56.0	1.20	12.61 ± 0.01	-2 ± 10	37.63	0.2000 ± 0.0003	0.3794 ± 0.0003	0.0965 ± 0.0008	3.69	-5.118 ± 0.008

APPENDIX C: ALLESFITTER RESULTS TABLES

Here we present the full set of fitted (Table C1) and derived (Table C2) parameters of NGTS-38 b produced by ALLESFITTER (see Section 5). Some of these parameters are repeated in Table 3. These will be available online in a machine readable format.

This paper has been typeset from a $\text{\TeX}/\text{\LaTeX}$ file prepared by the author.

Table C1. ALLESFITTER global fitted values and priors.

Parameter	Initial guess	Prior	Fitted value	units
<i>Astrophysical parameters</i>				
R_b/R_\star	0.06	$\mathcal{U}(0, 0.1)$	0.05909 ± 0.00061	
$(R_\star + R_b)/a_b$	0.014	$\mathcal{U}(0, 0.05)$	0.01332 ± 0.00037	
$\cos i_b$	0.009	$\mathcal{U}(0, 1)$	0.00825 ± 0.00033	
$T_{0;b}$	2459209.228	$\mathcal{U}(2459208, 2459210)$	2459209.2286 ± 0.0031	BJD
P_b	180.5	$\mathcal{U}(179, 181)$	180.52791 ± 0.00038	days
$\sqrt{e_b} \cos \omega_b$	0.1	$\mathcal{U}(-1, 1)$	0.0783 ± 0.0058	
$\sqrt{e_b} \sin \omega_b$	-0.5	$\mathcal{U}(-1, 1)$	-0.5493 ± 0.010	
K_b	0.14	$\mathcal{U}(0, 0.5)$	0.1372 ± 0.0018	km s^{-1}
<i>Instrumental limb darkening parameters</i>				
$q_{1;\text{TESS}}$	0.278	$\mathcal{N}(0.278, 0.002)$	0.2782 ± 0.0019	
$q_{2;\text{TESS}}$	0.375	$\mathcal{N}(0.375, 0.025)$	0.385 ± 0.024	
$q_{1;\text{NGTS}}$	0.337	$\mathcal{N}(0.337, 0.003)$	0.3368 ± 0.0027	
$q_{2;\text{NGTS}}$	0.385	$\mathcal{N}(0.385, 0.025)$	$0.385^{+0.023}_{-0.024}$	
$q_{1;\text{LCO}}$	0.283	$\mathcal{N}(0.283, 0.003)$	0.2827 ± 0.0029	
$q_{2;\text{LCO}}$	0.379	$\mathcal{N}(0.379, 0.026)$	$0.373^{+0.023}_{-0.025}$	
$q_{1;\text{ElSauce}}$	0.376	$\mathcal{N}(0.376, 0.009)$	0.3750 ± 0.0085	
$q_{2;\text{ElSauce}}$	0.388	$\mathcal{N}(0.388, 0.073)$	0.381 ± 0.067	
$q_{1;\text{DSC0.4m}}$	0.337	$\mathcal{N}(0.337, 0.009)$	0.3376 ± 0.0086	
$q_{2;\text{DSC0.4m}}$	0.384	$\mathcal{N}(0.384, 0.076)$	0.372 ± 0.071	
$q_{1;\text{OACC-CAO}}$	0.269	$\mathcal{N}(0.269, 0.008)$	0.2689 ± 0.0076	
$q_{2;\text{OACC-CAO}}$	0.376	$\mathcal{N}(0.376, 0.079)$	0.382 ± 0.073	
<i>Instrumental white noise parameters</i>				
$\ln \sigma_{\text{TESS}}$	-6.0	$\mathcal{U}(-14.0, 0.0)$	-7.750 ± 0.011	$\ln \text{rel.flux.}$
$\ln \sigma_{\text{NGTS}}$	-6.0	$\mathcal{U}(-14.0, 0.0)$	-4.900 ± 0.011	$\ln \text{rel.flux.}$
$\ln \sigma_{\text{LCO-CTIO(1m)}}$	-6.0	$\mathcal{U}(-14.0, 0.0)$	-6.250 ± 0.020	$\ln \text{rel.flux.}$
$\ln \sigma_{\text{LCO-CTIO(0.35m)}}$	-6.0	$\mathcal{U}(-14.0, 0.0)$	-5.749 ± 0.026	$\ln \text{rel.flux.}$
$\ln \sigma_{\text{LCO-SSO(1m)}}$	-6.0	$\mathcal{U}(-14.0, 0.0)$	-6.668 ± 0.022	$\ln \text{rel.flux.}$
$\ln \sigma_{\text{LCO-SSO(0.35m)}}$	-6.0	$\mathcal{U}(-14.0, 0.0)$	-5.966 ± 0.020	$\ln \text{rel.flux.}$
$\ln \sigma_{\text{ElSauce}}$	-6.0	$\mathcal{U}(-14.0, 0.0)$	-5.134 ± 0.025	$\ln \text{rel.flux.}$
$\ln \sigma_{\text{DSC0.4m}}$	-6.0	$\mathcal{U}(-14.0, 0.0)$	-6.251 ± 0.063	$\ln \text{rel.flux.}$
$\ln \sigma_{\text{OACC-CAO}}$	-6.0	$\mathcal{U}(-14.0, 0.0)$	$-6.153^{+0.048}_{-0.046}$	$\ln \text{rel.flux.}$
$\ln \sigma_{\text{CORALIE14}}$	-5.0	$\mathcal{U}(-7.6, -4.6)$	$-6.32^{+0.91}_{-0.81}$	$\ln \text{km s}^{-1}$
$\ln \sigma_{\text{CORALIE24}}$	-5.0	$\mathcal{U}(-7.6, -4.6)$	$-6.21^{+0.96}_{-0.90}$	$\ln \text{km s}^{-1}$
$\ln \sigma_{\text{HARPS}}$	-5.0	$\mathcal{U}(-7.6, -4.6)$	$-5.40^{+0.30}_{-0.39}$	$\ln \text{km s}^{-1}$
<i>Instrumental red noise / offset parameters</i>				
offset CORALIE14	20.03	$\mathcal{U}(19.95, 20.05)$	20.0357 ± 0.0046	km s^{-1}
offset CORALIE24	20.03	$\mathcal{U}(19.95, 20.05)$	20.0315 ± 0.0031	km s^{-1}
offset HARPS	19.93	$\mathcal{U}(19.9, 20.0)$	19.9306 ± 0.0014	km s^{-1}
offset NGTS	-0.0005	$\mathcal{U}(-0.001, 0.001)$	-0.00034 ± 0.00011	
offset LCO-CTIO (1m)	0.0	$\mathcal{U}(-0.001, 0.001)$	-0.000327 ± 0.000068	
offset LCO-CTIO (0.35m)	0.0	$\mathcal{U}(-0.001, 0.001)$	-0.00032 ± 0.00012	
offset LCO-SSO (1m)	0.0	$\mathcal{U}(-0.001, 0.001)$	0.000025 ± 0.000042	
offset LCO-SSO (0.35m)	0.0	$\mathcal{U}(-0.001, 0.001)$	$-0.000048^{+0.000076}_{-0.000071}$	
offset ElSauce	0.0	$\mathcal{U}(-0.001, 0.001)$	-0.00057 ± 0.00020	
offset DSC0.4m	0.0	$\mathcal{U}(-0.001, 0.001)$	$-0.00066^{+0.00018}_{-0.00017}$	
offset OACC-CAO	0.0	$\mathcal{U}(-0.001, 0.001)$	-0.00065 ± 0.00015	

Table C2. ALLESFITTER global model derived values.

Parameter	Value	Unit
<i>Astrophysical parameters</i>		
R_\star/a_b	0.01258 ± 0.00035	
a_b/R_\star	$79.5^{+2.2}_{-2.1}$	
R_b/a_b	0.000743 ± 0.000026	
R_b	12.12 ± 0.53	R_\oplus
R_b	1.081 ± 0.047	R_J
a_b	149.5 ± 7.7	R_\odot
a_b	0.695 ± 0.036	au
i_b	89.528 ± 0.019	deg
e_b	0.308 ± 0.011	
ω_b	278.11 ± 0.70	deg
q_b	$0.00313^{+0.00017}_{-0.00016}$	
M_b	1520^{+130}_{-120}	M_\oplus
M_b	$4.78^{+0.40}_{-0.37}$	M_J
M_b	$0.00456^{+0.00038}_{-0.00036}$	M_\odot
$b_{\text{tra};b}$	$0.8540^{+0.0090}_{-0.010}$	
$T_{\text{tot};b}$	14.88 ± 0.13	hours
$T_{\text{full};b}$	$9.38^{+0.27}_{-0.29}$	hours
ρ_\star	$0.292^{+0.025}_{-0.022}$	cgs
ρ_b	$4.69^{+0.95}_{-0.78}$	cgs
g_b	9510^{+700}_{-630}	cgs
$T_{\text{eq};b}$	458 ± 11	K
<i>Transit depth per Instrument</i>		
$\delta_{\text{tr};b;TESS}$	3.200 ± 0.051	parts per thousand (ppt)
$\delta_{\text{tr};b;NGTS}$	3.169 ± 0.050	parts per thousand (ppt)
$\delta_{\text{tr};b;LCO-SSO1m}$	3.206 ± 0.052	parts per thousand (ppt)
$\delta_{\text{tr};b;LCO-SSO0.35m}$	$3.207^{+0.054}_{-0.051}$	parts per thousand (ppt)
$\delta_{\text{tr};b;LCO-CTIO1m}$	$3.203^{+0.056}_{-0.045}$	parts per thousand (ppt)
$\delta_{\text{tr};b;LCO-CTIO0.35m}$	3.205 ± 0.049	parts per thousand (ppt)
$\delta_{\text{tr};b;ElSauce}$	3.154 ± 0.062	parts per thousand (ppt)
$\delta_{\text{tr};b;DSCO.4m}$	3.175 ± 0.065	parts per thousand (ppt)
$\delta_{\text{tr};b;OACC-CAO}$	3.212 ± 0.060	parts per thousand (ppt)
<i>Classical limb darkening parameters per instrument</i>		
$u_1;TESS$	0.406 ± 0.026	
$u_2;TESS$	0.121 ± 0.025	
$u_1;NGTS$	0.447 ± 0.028	
$u_2;NGTS$	0.134 ± 0.028	
$u_1;LCOGT$	$0.397^{+0.024}_{-0.026}$	
$u_2;LCOGT$	$0.135^{+0.026}_{-0.024}$	
$u_1;ElSauce$	0.466 ± 0.083	
$u_2;ElSauce$	0.146 ± 0.083	
$u_1;DSCO.4m$	0.432 ± 0.083	
$u_2;DSCO.4m$	0.149 ± 0.083	
$u_1;OACC-CAO$	$0.397^{+0.073}_{-0.077}$	
$u_2;OACC-CAO$	0.122 ± 0.076	